A method for assessing model extensions: Application to modelling winter precipitation with a microscale obstacle-resolving meteorological model (MITRAS v4.0)

Karolin S. Samsel[1,2], Marita Boettcher[2], David Grawe[2], K. Heinke Schlünzen[2], and Kevin Sieck[1]

[1]Climate Service Center Germany (GERICS), Helmholtz-Zentrum Hereon, Chilehaus, Fischertwiete 1, 20095 Hamburg, Germany

[2]Meteorological Institute, Center for Earth System Research and Sustainability (CEN), University of Hamburg, Hamburg, Germany

Correspondence: Karolin S. Samsel (karolin.samsel@uni-hamburg.de)

Abstract. The microscale, obstacle-resolving meteorological transport and stream model MITRAS has been extended with a snow cover and precipitation scheme. The performance of the model extension is assessed by comparing the results of different model versions using a method based on hit rates originally developed for assessing wind performance. For temperature, radiation and precipitation, estimates for the threshold values were derived based on computational accuracy; these are used in the

5   hit rate calculation for these variables. The threshold values for the deviations are $0.02\,\mathrm{ms}^{-1}$ (5 %) for the wind components, $0.05\,\mathrm{K}$ (0.02 %) for temperature, $0.5\,\mathrm{Wm}^{-2}$ (0.5 %) and $0.5\,\mathrm{Wm}^{-2}$ (0.2 %) for the net long and short wave radiation, and $0.001\,\mathrm{mm}$ (1 %) for precipitation on ground. The model extensions produce plausible results and better represent winter precipitation. This opens the opportunity to study with higher accuracy the influence of obstacles on precipitation heterogeneities.

1 Introduction

10   Climate change related impacts on the urban climate in winter situations are usually investigated focusing on cities in high-latitude or cold climate regions, where high snow loads are expected. Multiple studies based on measuring campaigns were performed on the influence of snow on, e.g., the Urban Heat Island in Minneapolis (USA) (Malevich and Klink, 2011), in the Twin Cities metropolitan area (Minneapolis-St. Paul, USA) (Smoliak et al., 2015), or in Madison (USA) (Schatz and Kucharik, 2014). Special focus on the impact of snow cover and snow melt on the surface energy balances was laid in studies for example

15   in Montreal (Canada) (Lemonsu et al., 2008, 2010; Bergeron and Strachan, 2012), in Calgary (Canada) (Ho and Valeo, 2005), or in Harbin (China) (Shui et al., 2019). Also, numerical examinations were carried out for example for Sapporo (Japan) (Mori and Sato, 2015) or for Yichun (China) (Shui et al., 2016).

    Investigating the influence of urban areas on patterns of rainfall (Hu et al., 2024; Lu et al., 2024; Zhang et al., 2022; Liu and Niyogi, 2019) and snowfall (Salvi and Kumar, 2024) received more and more interest in the scientific community. Local scale

20   influences of obstacles on the heterogeneity of snow has been investigated using wind tunnel experiments with focus on urban block designs (Watanabe et al., 2017), or on the interference of high-rise buildings on the snow load on a low-rise building (Zhang et al., 2021), or on snowdrift on flat roofs during snowfall (Zhou et al., 2021).

Increasing computational power allows the use of high resolution in modelling. In numerical models, fit-for-purpose microphysical schemes are used to model precipitation processes depending on the scale of the model. At global scales, simple

25   schemes with one ice phase are applied (Roeckner et al., 2003). The sedimentation of falling hydrometeors is often neglected, i.e. precipitation is falling from the cloud to the surface in one time step, because the numerical time step is large enough to justify this assumption. With increasing resolution, more elaborated schemes are used. Typical regional weather and climate models use multi-moment schemes (e.g., Doms et al., 2011) and take into account e.g. evaporation of rain during sedimentation over several time steps, which requires special treatment of the sedimentation in order to keep numerical stability (e.g.,

30   Bouteloup et al., 2011; Doms et al., 2011; Geleyn et al., 2008).

Available obstacle-resolving models do not yet commonly consider precipitation. The microscale model MITRAS, for instance, includes a precipitation scheme (Ferner et al., 2022). The obstacle-resolving high-resolution urban climate model PALM-4U, which is based on PALM (Maronga et al., 2020), does not include precipitation, yet (Maronga et al., 2019). The Regional Atmospheric Modeling System (RAMS) (Pielke et al., 1992) includes a parameterisation for cloud processes and has

35   also been used for flow simulations around obstacles (Castelli and Reisin, 2010), but no investigations of precipitation within urban neighbourhoods were performed.

Studies specifically focusing on the influence of obstacles on snow are predominantly conducted for snow climate cities. Less severe snowfall occurs in warm temperate climate cities like Hamburg (Germany) (Meinke et al., 2018); it still influences e.g. pedestrian comfort due to icy grounds or public transport due to snow covered bus stops. For these smaller snow loads,

40   other processes might have a stronger influence on the heterogeneity of snow than for the high loads. Information on snow heterogeneities within an urban area are a useful first step for analyses concerning frost heterogeneities or human comfort. To our knowledge, there is no obstacle-resolving model currently available that includes both rain and snow. In this paper, a description of the implemented winter precipitation scheme in the obstacle-resolving model MITRAS (Schlünzen et al., 2003; Salim et al., 2018) is provided as well as plausibility tests and their results to assess the reliability of the new scheme. The

45   implemented processes are included in MITRAS v4.0, which also includes other developments.

A short description of MITRAS v3.0 is given in Sect. 2. The model extensions for MITRAS v3.1 concerning the diffusion of scalars and the newly introduced boundary conditions for rain on building surfaces are described in Sect. 3. The representation of snow cover and the adjustments made for scale and obstacles for MITRAS v3.3 can be found in Sect. 4. Note, that the model extensions for MITRAS v3.2 (Badeke et al., 2021) are not within the scope of this paper. The extension of the cloud

50   microphysics is described in Sect. 5. The changes to the model are tested for plausibility by comparing the above-mentioned model versions in Sect. 6. Finally, conclusions and outlook are given in Sect. 7.

2   Obstacle-resolving model MITRAS

The three-dimensional, non-hydrostatic, prognostic, **MI**croscale, obstacle-resolving **TRA**nsport and **S**tream model **MITRAS** is part of the M-SYS model system (Trukenmüller et al., 2004; Schatzmann et al., 2006). The basic equations are written in

55   flux form, transformed into a terrain-following coordinate system, $\dot{x}^1$, $\dot{x}^2$, $\dot{x}^3$, and filtered using Reynolds averaging (Salim

et al., 2018). As a consequence, the atmospheric state variables are divided into an average value over a finite time and grid volume and its deviation. For scalar quantities ϕ such as temperature or humidity the average value is further decomposed into a basic state value, ϕ_0, and its microscale deviation, $\tilde{\phi}$ (Pielke, 2013).

The equations are numerically solved on an Arakawa C grid (Arakawa and Lamb, 1977). Scalar quantities such as tem-
60   perature or cloud and rain water content are defined at grid cell centres (scalar points), whereas the u-wind is defined at the x-boundaries of the grid cell, the v-wind at the y-boundaries, and the w-wind at the vertical (z) boundaries; these are named vector grid points. Obstacle surfaces are positioned at vector grid points. Obstacles are simulated by assuming impermeable grid cells at the building position using 3-D fields of weighting factors. The weighting factors contain the information whether a grid cell lies in the atmosphere or in a building. Weighting factors are additionally used to define whether a grid cell's boundary
65   denotes a building face (Briscolini and Santangelo, 1989; Mittal and Iaccarino, 2005).

The solved prognostic equation for a scalar quantity includes advection, diffusion $\overline{F_{\overline{\phi}}}$ (Eq. 1) containing the subgrid-scale turbulent fluxes, as well as sources and sinks (Schlünzen et al., 2018a; Salim et al., 2018). The subgrid-scale fluxes of scalars mathematically result from averaging the model equations. The flux terms prevent closing the coupled nonlinear equations system. Consequently, solutions to this so-called "closure problem" are needed, which are presented in Section 2.1. The cloud
70   microphysics parameterisation for warm rain is given Section 2.2. As the model is well documented (Salim et al., 2018; Schlünzen et al., 2018a; Fischereit, 2018), only a brief description of those parts of MITRAS v3.0, that will be extended, are provided in the following. The model extensions are given in Sects. 3 to 5.

2.1 Diffusion term

The diffusion term is given in the terrain-following coordinate system as

$$
\begin{aligned}
75 \quad \overline{F_{\overline{\phi}}} = {} & \frac{\partial}{\partial \dot{x}^1} \left(\alpha^* \rho_0 \overline{u'\phi'} \frac{\partial \dot{x}^1}{\partial x} \right) + \frac{\partial}{\partial \dot{x}^2} \left(\alpha^* \rho_0 \overline{v'\phi'} \frac{\partial \dot{x}^2}{\partial y} \right) \\
& + \frac{\partial}{\partial \dot{x}^3} \left(\alpha^* \rho_0 \overline{u'\phi'} \frac{\partial \dot{x}^3}{\partial x} + \alpha^* \rho_0 \overline{v'\phi'} \frac{\partial \dot{x}^3}{\partial y} + \alpha^* \rho_0 \overline{w'\phi'} \frac{\partial \dot{x}^3}{\partial z} \right)
\end{aligned}
\tag{1}
$$

with the grid volume α^*, the basic state atmospheric density ρ_0, the wind velocity components u, v, w, and Cartesian coordinates x, y, z. The fluxes are parameterised using a first-order closure

$$-\rho_0\overline{u'\phi'} = \rho_0 K_{\text{hor}} \left(\frac{\partial\overline{\phi}}{\partial\dot{x}^1} \frac{\partial\dot{x}^1}{\partial x} + \frac{\partial\overline{\phi}}{\partial\dot{x}^3} \frac{\partial\dot{x}^3}{\partial x} \right) \tag{2}$$

$$-\rho_0\overline{v'\phi'} = \rho_0 K_{\text{hor}} \left(\frac{\partial\overline{\phi}}{\partial\dot{x}^2} \frac{\partial\dot{x}^2}{\partial y} + \frac{\partial\overline{\phi}}{\partial\dot{x}^3} \frac{\partial\dot{x}^3}{\partial y} \right) \tag{3}$$

$$-\rho_0\overline{w'\phi'} = \rho_0 K_{\text{ver}} \left(\frac{\partial\overline{\phi'}}{\partial\dot{x}^3} \frac{\partial\dot{x}^3}{\partial z} \right) \tag{4}$$

with the horizontal and vertical exchange coefficients K_{hor} and K_{ver}, respectively (Schlünzen et al., 2018a; Salim et al., 2018). Inserting the expressions for the subgrid-scale turbulent fluxes (Eqs. 2-4) into the diffusion term (Eq. 1) leads to the equations as used in the prior model version MITRAS v3.0 (Salim et al., 2018; Schlünzen et al., 2018a; Fischereit, 2018).

2.2 Microphysics for warm clouds

In the M-SYS model system (Schlünzen et al., 2018a), a Kessler-type parameterisation (Kessler, 1969) is applied (Köhler, 1990). It is a three-category (water vapour q_1^1, cloud water q_1^{2c}, and rain water q_1^{2r}) bulk water-continuity model designed for warm clouds (Doms, 1985; Köhler, 1990). In Sect. 5 Fig. 3, the processes included in the warm scheme are shown in grey and black.

Liquid water drops in the atmosphere are distinguished by their droplet size. Drops with a mean drop radius of about $10\,\mu\text{m}$ are considered cloud water, whereas drops with a mean radius of about $100\,\mu\text{m}$ are defined as rain water. The separation radius is $40\,\mu\text{m}$ (Schlünzen et al., 2018a). For rain drops, the Marshall-Palmer size distribution (Marshall and Palmer, 1948) is assumed.

A terminal velocity is the mass weighted mean of the individual sedimentation speeds. The following expression for the terminal velocity of rain, v_{TR}, is used (Köhler, 1990; Schlünzen et al., 2018a)

$$v_{\text{TR}} = 68.81 \frac{\text{m}}{\text{s}} \left(\frac{\text{m}^3}{\text{kg}} \right)^{0.1905} \cdot \left(10^{-3} \cdot \rho_0 q_1^{2r} \right)^{0.1905} \tag{5}$$

which is taken from Doms (1985), recalculated to SI-units. To take the smaller densities at higher altitudes into account, a correction factor

$$F = \sqrt{\frac{\rho_{\text{ref}}}{\rho_0}} \tag{6}$$

with the reference density $\rho_{\text{ref}} = 1.29\,\text{kg}\,\text{m}^{-3}$ is included. The terminal velocity is thus larger for larger altitudes.

The coagulation of cloud water drops leads to new rain water drops, which is called autoconversion. For the autoconversion

105 process to start, enough cloud drops that are big enough to allow coagulation have to be present (Doms, 1985). The critical

value is taken as $q_{1,\text{cri}}^{2c} = 10^{-3}\,\text{kg}\,\text{kg}^{-1}$. Above the critical value, rain water production depends linearly on the cloud water

content with the inverse autoconversion interval $k_{\text{warm}}^{\text{r}} = 10^{-3}\,\text{s}^{-1}$. Consequently, the autoconversion rate for the warm rain

scheme is

$$B_{\text{au}}^{\text{w}} = \max\left(0, k_{\text{warm}}^{\text{r}} \cdot \left(q_1^{2c} - q_{1,\text{cri}}^{2c}\right)\right) \tag{7}$$

110 (Köhler, 1990; Schlünzen et al., 2018a).

Accretion is the growth of rain drops by collecting cloud drops. The parameterisation of this process is based on the continuous model for droplet growth. It assumes a uniform and continuous distribution of cloud drops, as well as that their radii are much smaller than the rain drop radii and that the cloud drop sedimentation speed is zero (Doms, 1985). This leads to the accretion equation

$$115 \quad B_{\text{acc}}^{\text{w}} = \frac{934.63}{\text{s}} \left(\frac{\text{m}^3}{\text{kg}}\right)^{0.875} \cdot q_1^{2c} \cdot \left(10^{-3} \cdot \rho_0 \cdot q_1^{2r}\right)^{0.875} \tag{8}$$

(Köhler, 1990; Schlünzen et al., 2018a) which is the original equation by Doms (1985) converted to SI units.

The calculation of condensation and evaporation to and from cloud droplets is based on the method of saturation adjustment (Asai, 1965). It assumes that within a cloud, saturation is achieved. The sedimentation flux of cloud droplets is neglected. If the humidity exceeds the saturation specific humidity $q_{1,\text{sat}}^1$, condensation is

$$120 \quad B_{\text{cond}} = \frac{q_1^1 - q_{1,\text{sat}}^1}{\alpha_{\text{cond}}} \tag{9}$$

with the condensation parameter

$$\alpha_{\text{cond}} = 1 + \frac{L_{21} \cdot q_{1,\text{sat}}^1 \cdot 4028\,\text{K}}{c_{\text{p}} \cdot \left(T \cdot \left(\frac{p_0}{p_{\text{s}}}\right)^{\frac{R}{c_{\text{p}}}} - 38.33\,\text{K}\right)^2} \tag{10}$$

with the latent heat of vaporisation L_{21}, the specific heat for dry air c_{p}, temperature T, basic state pressure p_0, the ground surface pressure p_{S}, and the gas constant for dry air R (Köhler, 1990; Schlünzen et al., 2018a).

125 In the sub-saturated areas below the cloud, evaporation of rain water may occur. The evaporation is given as

$$B_{\text{evap}} = A_{\text{t}} \cdot \sqrt{\rho_0 \cdot 10^{-3} \cdot q_1^{2r}} \cdot F_{\text{v}} \cdot \frac{S}{\rho_0 \cdot 10^{-3}} \tag{11}$$

with saturation S and the parameter for the rain droplet spectrum

$$A_\mathrm{t} = \frac{2.623 \cdot 10^{-3} \left(\frac{\mathrm{m^3}}{\mathrm{kg}}\right)^{0.5} \frac{1}{\mathrm{s}} \cdot \left(\rho_0 \cdot 10^{-3} \cdot q_{1,\mathrm{sat}}^1\right)}{1 + 1.282 \cdot 10^{10} \, \frac{\mathrm{m^3 K^2}}{\mathrm{kg}} \cdot \left(\rho_0 \cdot 10^{-3} \cdot q_{1,\mathrm{sat}}^1\right) \theta^{-2}} \tag{12}$$

and the ventilation factor

130
$$F_\mathrm{v} = 0.78 + 80.73 \left(\frac{\mathrm{kg}}{\mathrm{m^3}}\right)^{-0.225} \cdot \left(\rho_0 \cdot 10^{-3} \cdot q_1^{2\mathrm{r}}\right)^{0.225} \tag{13}$$

(Köhler, 1990; Schlünzen et al., 2018a). The potential temperature is given as θ.

The influence of liquid water on radiation is included in the radiation parameterisation in MITRAS (Schlünzen et al., 2018a; Fischereit, 2018; Uphoff, 2019). There are two radiation schemes implemented: the two-stream approach and the vertically integrated approach, which does not consider clouds. Thus, only the two-stream approach can be applied when atmospheric

135 liquid water is present. For the long wave radiation, cloud and rain water is included in the calculation of the absorption coefficient. For the short wave radiation, only small droplets like cloud water are taken into account when deriving scattering and absorption by liquid water (Uphoff, 2019).

3 Modification of turbulent scalar fluxes

The cloud microphysics parameterisation (Sect. 2.2) was implemented in the mesoscale sister model METRAS (Schlünzen

140 et al., 2018a; Köhler, 1990), which does not resolve obstacles. To include liquid water contents in MITRAS, adjustments are made for the diffusion at obstacle surfaces, which apply to all scalar quantities (Sect. 3.1). Additionally, boundary conditions for cloud, rain and snow water content at obstacles are introduced (Sect. 3.2).

3.1 Changes in the model domain

The horizontal subgrid-scale fluxes depend on both the grid surface parallel gradient of ϕ (first terms in brackets on the right

145 hand side in Eqs. 2 and 3), and on the vertical gradients (second terms in brackets). The latter result from the transformation into the terrain-following coordinate system. However, the terrain-following coordinates create some numerical problems at obstacle walls. To explain these, the calculation of the diffusion in x-direction of e.g. liquid water content in a terrain-following grid cell will serve as an example (Fig. 1). An obstacle cell (shaded grey) is assumed below and in x-direction of the grid cell for which the diffusion is calculated (thick black boundary). The diffusion in x- direction following Eqs. (1)-(3) results in

150
$$\overline{F}_{\overline{\phi},\dot{x}^1} = -\frac{\partial}{\partial \dot{x}^1} \left(\alpha^* \rho_0 K_\mathrm{hor} \frac{\partial \overline{\phi}}{\partial \dot{x}^1} \frac{\partial \dot{x}^1}{\partial x} \frac{\partial \dot{x}^1}{\partial x} + \alpha^* \rho_0 K_\mathrm{hor} \frac{\partial \overline{\phi}}{\partial \dot{x}^3} \frac{\partial \dot{x}^3}{\partial x} \frac{\partial \dot{x}^1}{\partial x} \right). \tag{14}$$

The diffusion is the grid following gradient $\partial/\partial \dot{x}^1$ of the fluxes through the vertical grid cell boundaries (purple and grey arrow in Fig. 1). With a building at the right hand side of the grid cell, the flux is not calculated following Eq. (14). Instead, a specific building surface flux is applied (Sect. 3.2).
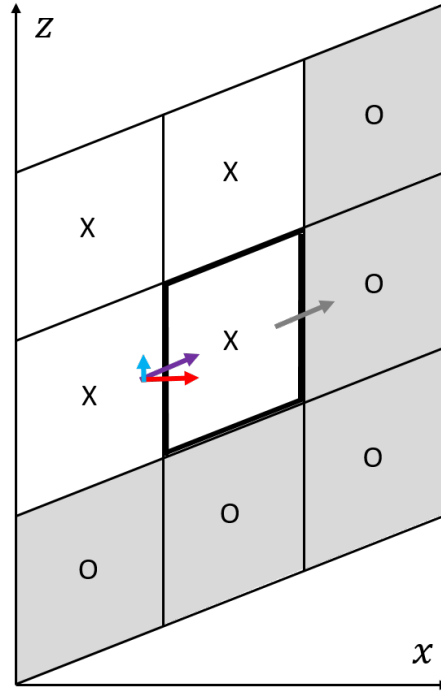
Figure 1. Example for the calculation of the diffusion in x-direction (violet and grey arrow parallel to grid cell boundaries) in a grid cell (thick black boundary) prior to model enhancements. The diffusive fluxes including the horizontal and vertical gradient of the scalar quantity are represented by the red and blue arrow. The grey arrow represents the obstacle surface flux. Obstacle cells are grey. Scalar quantities are defined at the crosses (atmospheric grid cells) and circles (building grid cells).

For the calculation of the fluxes between atmospheric grid cells, the grid following gradient $\partial/\partial\dot{x}^1$ and vertical gradients
155 of ϕ are required. The first term in brackets is represented as the violet arrow and the second as the blue arrow in Fig. 1. The calculation of the grid following $\partial/\partial\dot{x}^1$ gradient of ϕ is straight forward using the values of ϕ located at the grid cell centres left and right from the grid cell boundary (crosses in the central and middle left grid cell in Fig. 1). For the calculation of the vertical gradient, however, values of ϕ from all six grid cells that surround the grid cell boundary are used (two left columns of grid cells). This includes in the example provided in Fig. 1 two building grid cells (grey), which give no physically useful
160 values. When the horizontal diffusion is calculated, only fluxes through vertical walls are taken into account.

In general, the orography in MITRAS with the resolution of a few metres is relatively flat. Therefore, the second term in brackets in Eq. (14), which includes the slope of the terrain as $\partial\dot{x}^3/\partial x$, is small. By neglecting the influence of terrain steepness in the horizontal flux, Eq. (14) simplifies to only the first term. Similar simplifications can be done for the diffusion in the y-direction. This leads to the following expressions for the horizontal turbulent fluxes:

165

$$-\rho_0 \overline{u'\phi'} = \rho_0 K_{\text{hor}} \frac{\partial \overline{\phi}}{\partial \dot{x}^1} \frac{\partial \dot{x}^1}{\partial x} \tag{15}$$

$$-\rho_0 \overline{v'\phi'} = \rho_0 K_{\text{hor}} \frac{\partial \overline{\phi}}{\partial \dot{x}^2} \frac{\partial \dot{x}^2}{\partial y}. \tag{16}$$

3.2 Changes at obstacle surfaces

170 Boundary fluxes had been defined before for all scalar quantities at obstacle surfaces, except for cloud, rain and snow water content. For MITRAS, those quantities are added and the treatment of building surface fluxes at obstacle surfaces is adapted for all scalar quantities.

Previously, building surface fluxes for $\rho_0 \overline{u'\phi'}$, $\rho_0 \overline{v'\phi'}$, and $\rho_0 \overline{w'\phi'}$ were defined as a three-dimensional variable located at scalar grid points. Wall orientation was taken into account in the calculation of the building surface fluxes, but when more than 175 one building surface was present, only the value that has been calculated last was stored in the variable. For the example of a building edge as in Fig. 1, the same building surface flux was used for the vertical wall (grey arrow) as for the roof below (bottom boundary of central grid cell). Therefore, the structure of the building surface flux variables has been adjusted for all scalar quantities. Like other building surface variables (e.g. building surface temperature), a value is defined for each obstacle adjacent atmospheric grid cell and for each wall orientation. For the calculation of the pre-existing building surface fluxes, 180 boundary conditions as described in Salim et al. (2018); Schlünzen et al. (2018a) are applied.

For liquid water at the ground surface, the model allows for three surface boundary conditions: zero gradient, prescribed fixed value, and flux at the boundary equal to flux in the atmosphere above. For obstacle surfaces, the latter is chosen. Water and snow reaching a building close to the wall is considered to be absorbed by the adjacent surface. Considering again the configuration in Fig. 1: In order to get the building surface flux at the obstacle wall in positive x-direction of the atmospheric 185 grid cell (grey arrow), the flux at the opposite grid cell boundary is used, calculated following Eqs. (1) and (15) (Ferner et al., 2022). The same approach is applied for other wall directions and for cloud, rain and snow water content.

4 Consideration of a snow cover scheme in MITRAS

The microscale model MITRAS' mesoscale sister model METRAS (Trukenmüller et al., 2004; Schatzmann et al., 2006; Schlünzen et al., 2018a) includes a snow cover scheme, which is described in Boettcher (2017). In the present study, a similar 190 approach has been adapted in MITRAS. In METRAS, the snow cover scheme is only used when flux aggregation with the blending height concept is applied (von Salzen et al., 1996). In MITRAS, however, the effects of surface fractions and corresponding subgrid-scale fluxes are significantly lower due to the small grid cell sizes. Therefore, using the parameter averaging method is suitable (Schlünzen et al., 2018a) and the snow cover scheme is adapted to it. Additional adjustments are made for the consideration of obstacles, as well as for the smaller time spans and time steps of MITRAS model runs.

4.1 Surface energy budget at the ground

Without snow, the change of temperature at ground surface, $T_{\rm S}$, with time t is calculated following Eq. (17) in MITRAS considering net short and long wave radiation $SW_{\rm net}$ and $LW_{\rm net}$, sensible and latent heat fluxes $H_{\rm S}$ and $L_{\rm S}$, heat flux to and from the soil at the surface $G_{\rm soil}$ (Eq. 19), using thermal diffusivity $k_{\rm soil}$, thermal conductivity $\nu_{\rm soil}$, and deep soil temperature $T_{\rm h,soil}$ at the depth $h_{\rm soil}$.

$$\frac{\partial T_{\rm S}}{\partial t} = B^* \left(SW_{\rm net} + LW_{\rm net} + H_{\rm S} + L_{\rm S} + G_{\rm soil} \right) \tag{17}$$

with

$$B^* = 2\sqrt{\pi}\,\frac{k_{\rm soil}}{\nu_{\rm soil} h_{\rm soil}} \tag{18}$$

The soil heat flux $G_{\rm soil}$ (Eq. 19), is expressed using the force-restore method (Bhumralkar, 1975; Deardorff, 1978). The deep soil temperature can be assumed constant for shorter time ranges (< 3 days).

$$G_{\rm soil} = -\sqrt{\pi} \left(\frac{h_{\rm soil}}{\nu_{\rm soil}} \right)^{-1} \left(T_{\rm S}(t) - T_{\rm h,soil} \right) \tag{19}$$

In case of snow on ground, an additional snow layer is assumed, which impacts the temperature on and near the ground surface as described for METRAS in Boettcher (2017). The treatment of the snow layer is based on Hirota et al. (2002). The thermal diffusivity of snow $k_{\rm snow}$ is given in Eq. (20) using the snow volumetric heat capacity $c_{\rm v,snow}$ (Eq. 21). The snow thermal conductivity $\nu_{\rm snow}$ (Eq. 22) and volumetric heat capacity $c_{\rm v,snow}$ both depend on the density of the snow pack $\rho_{\rm snow}$ (Eq. 28). The snow thermal conductivity, the snow volumetric heat capacity, and the depth of the temperature wave into the snow are given in Eqs. (22)-(23) using the specific heat capacity of ice $c_{\rm ice}$, the density of ice $\rho_{\rm ice}$, the thermal conductivity of ice $\nu_{\rm ice}$, and the period of the temperature wave $\tau = 86400\,s = 1\,d$.

$$k_{\rm snow} = \frac{\nu_{\rm snow}}{c_{\rm v,snow}} \tag{20}$$

$$c_{\rm v,snow} = \frac{c_{\rm ice} \cdot \rho_{\rm snow}}{\rho_{\rm ice}} \tag{21}$$

$$\nu_{\rm snow} = \nu_{\rm ice} \cdot \left(\frac{\rho_{\rm snow}}{\rho_{\rm w}} \right)^{1.88} \tag{22}$$

$$h_{\rm snow} = \sqrt{\tau \cdot \frac{\nu_{\rm snow}}{c_{\rm v,snow}}} \tag{23}$$

The snow depth $z_{\rm snow}$ (Eq. 24) is calculated using the snow water equivalent SWE (Eq. 29) and the density of water $\rho_{\rm w}$.

$$z_{\rm snow} = SWE \cdot \frac{\rho_{\rm w}}{\rho_{\rm snow}} \tag{24}$$

Two cases form limit value situations which are to be treated as follows: In case of a shallow snow cover, meaning, the depth of the temperature wave into the snow h_{snow} (Eq. 23) exceeds the snow depth z_{snow} (Eq. 24), the heat conduction of snow cover and snow soil heat flux can be expressed with Eqs. (25) and (26) using Eq. (20).

$$B^* = 2\sqrt{\pi}\frac{1}{c_{\text{v,snow}}z_{\text{snow}}} \tag{25}$$

$$G_{\text{soil}} = -\sqrt{\pi}\left(\frac{z_{\text{snow}}}{\nu_{\text{snow}}} + \frac{h_{\text{soil}}}{\nu_{\text{soil}}}\right)^{-1} \cdot (T_{\text{S}}(t) - T_{\text{h,soil}}). \tag{26}$$

In case of a very thick snow cover, the heat wave does not reach below the snow and h_{soil} becomes zero leading to a soil heat flux of Eq. (27) (Boettcher, 2017). The heat conduction B^* is calculated following Eq. (25) but using the temperature depth in snow h_{snow} instead of the snow depth z_{snow}.

$$G_{\text{soil}} = -\sqrt{\pi}\left(\frac{h_{\text{snow}}}{\nu_{\text{snow}}}\right)^{-1}(T_{\text{S}}(t) - T_{\text{h,soil}}) \tag{27}$$

4.2 Snow density

As a snow pack ages, its density (Eq. 28) increases. Boettcher (2017) assumes an asymptotic solution with time from a minimum density ρ_{min} to a maximum density ρ_{max} with the empirical parameters τ_{f} and τ_1 and time step Δt following Verseghy (1991); Douville et al. (1995); Dutra et al. (2010).

$$\rho_{\text{snow}}(t + \Delta t) = (\rho_{\text{snow}}(t) - \rho_{\text{max}}) \cdot \exp\left(-\tau_{\text{f}}\frac{\Delta t}{\tau_1}\right) + \rho_{\text{max}} \tag{28}$$

The parameters were chosen according to Verseghy (1991) with $\rho_{\text{min}} = 100\,\text{kg m}^{-3}$, $\rho_{\text{max}} = 300\,\text{kg m}^{-3}$, $\tau_{\text{f}} = 0.24$ and $\tau_1 = 86400\,\text{s}$.

For the snow albedo (Sect. 4.5), the parameters suggested by Järvi et al. (2014) were chosen in the implementation of the obstacle-resolving microscale model over those suggested by Verseghy (1991) and Boettcher (2017), as they fit observations in an urban area better by considering anthropogenic pollution. For the snow density, however, we decided to keep the parameters suggested by Verseghy (1991). The parameterisation in MITRAS is supposed to represent a snow event in a city like Hamburg (Germany). The parameters suggested by Järvi et al. (2014) fit well for snow climate cities like Montreal or Helsinki, but they do not necessarily fit equally well for Hamburg, where larger snow packs are rare.

4.3 Snow water equivalent

The snow water equivalent SWE (Eq. 29) with the unit of metres represents the mass of snow using an equivalent water height. In contrast, the height of the snow pack is given in Eq. (24). The snow water equivalent is reduced by evaporation E and melting M_{snow} (Eq. 30). The rate of snowfall Pr_{snow} adds to it (Boettcher, 2017).

$$\frac{\partial SWE}{\partial t} = Pr_{\text{snow}} - E - M_{\text{snow}} \tag{29}$$

In Boettcher (2017), no precipitating snow is calculated. Rain reaching the ground is assumed to be snow, if the surface temperature is below the freezing point T_0. In MITRAS, precipitating snow is calculated (Sect. 5.1) and considered in the rate of snowfall. For simplicity, rain is assumed to be snow on ground for surface temperatures below the freezing point. Similarly, precipitating snow reaching the ground for temperatures above freezing point, is assumed to be rain in the calculation of the soil water content. Diffusive fluxes into the ground are only possible in the absence of a snow cover. As a consequence, for air temperatures above freezing point, with both snow and rain falling, the snow water equivalent might be overestimated, if the surface temperatures are below the freezing point.

Snow melt (Eq. 30) is calculated following Boettcher (2017) using the latent heat of fusion L_{32}.

$$M_{\text{snow}} = \frac{\nu_{\text{snow}}}{\rho_{\text{w}} L_{32} z_{\text{snow}}} (T_{\text{S}} - T_0) \tag{30}$$

4.4 Snow roughness length

The roughness length of snow-covered areas is reduced compared to snow-free areas as a snow pack smooths a surface. The roughness length z_0 under the influence of snow (Eq. 31) is calculated using the snow roughness length $z_{0_{\text{snow}}} = 10^{-3}$ m, the roughness length of areas without snow cover $z_{0_{\text{ini}}}$, and the snow cover fraction $p_{\text{snow}_{z_0}}$ (Eq. 32) following Boettcher (2017).

$$z_0 = (1 - p_{\text{snow}_{z_0}}) \cdot z_{0_{\text{ini}}} + p_{\text{snow}_{z_0}} \cdot z_{0_{\text{snow}}} \tag{31}$$

The parameterisation of the snow cover fraction (Eq. 32) is based on Douville et al. (1995) with the empirical factor $\beta = 0.408$.

$$p_{\text{snow}_{z_0}} = \frac{SWE}{SWE + \beta \cdot z_{0_{\text{ini}}}} \tag{32}$$

For now, the influence of snow cover on the roughness length of roofs is neglected. For obstacle surfaces including roofs, the roughness length for concrete ($z_0 = 10^{-3}$ m) is assumed regardless of snow cover.

4.5 Snow albedo

If there is already a snow pack present, the albedo α of the ground surface (Eq. 33) is increased to a maximum albedo α_{max} after one hour of snowfall with the magnitude $0.01\,\text{m}\,\text{h}^{-1}$, or an equivalent value is used, e.g. with a higher magnitude for 0.01 m of snow in a shorter time (Boettcher, 2017; Dutra et al., 2010). The amount of snowfall is represented by the change of the snow water equivalent ΔSWE.

$$\alpha(t + \Delta t) = \alpha(t) + \min\left(1, \frac{\Delta SWE \cdot 3600\,\mathrm{s}}{\Delta t \cdot 0.01\,\mathrm{m}}\right) \cdot (\alpha_{\mathrm{max}} - \alpha(t)) \tag{33}$$

Baker et al. (1991) found, that a minimum snow depth of $5\,\mathrm{cm}$ is required to completely mask the albedo of the underlying soil. The effect of the surface covers shining through the snow surface is included in MITRAS. However, in a city like Hamburg, which aims at black roads in winter, snow rarely remains untouched because of winter services and traffic, which means the albedo of the underlying soil (α_{ini}) shines through for snow depths greater than $5\,\mathrm{cm}$. These effects of direct human activities are included by using a basic approach. The underlying albedo is considered until a snow depth of $0.5\,\mathrm{m}$ is reached, then a snow cover of fresh snow is assumed. This is represented by a linear relation (Eq. 34) using the critical snow water equivalent $SWE_{\mathrm{crit}} = 0.05\,\mathrm{m}$, which corresponds a snow depth of $0.5\,\mathrm{m}$ (Eq. 24). In MITRAS, Eq. 33 is used for snow albedo in case of snowfall with snow water equivalent higher than SWE_{crit}. Eq. 34 is used for values below SWE_{crit} with and without snowfall because the impact of the underlying soil is assumed to be larger than the impact of aging of the snow pack.

$$\alpha = \alpha_{\mathrm{ini}} + \min\left(1, \frac{SWE}{SWE_{\mathrm{crit}}}\right) \cdot (\alpha_{\mathrm{max}} - \alpha_{\mathrm{ini}}) \tag{34}$$

Without snowfall and a snow water equivalent greater than SWE_{crit}, the albedo is simultaneously decreased due to the aging of the snow pack. For temperatures below the freezing point, a linear decrease of the albedo to the minimum albedo α_{min} is assumed (Eq. 35) and if it is warmer, an exponential decrease (Eq. 36) is assumed using the empirical factors τ_{α} and $\tau_{\mathrm{f},\alpha}$ following Verseghy (1991); Douville et al. (1995).

$$\alpha(t + \Delta t) = \alpha(t) - \tau_{\alpha} \cdot \frac{\Delta t}{\tau_1} \qquad\qquad \text{for } T_{\mathrm{S}} < 273.16\,\mathrm{K} \tag{35}$$

$$\alpha(t + \Delta t) = (\alpha(t) - \alpha_{\mathrm{min}}) \cdot \exp\left(-\tau_{\mathrm{f},\alpha} \cdot \frac{\Delta t}{\tau_1}\right) + \alpha_{\mathrm{min}} \qquad\qquad \text{for } T_{\mathrm{S}} > 273.16\,\mathrm{K} \tag{36}$$

For the mesoscale model METRAS, the parameters provided by Verseghy (1991) are applied with $\alpha_{\mathrm{min,V91}} = 0.5$, $\tau_{\alpha,\mathrm{V91}} = 0.008$, and $\tau_{\mathrm{f},\alpha,\mathrm{V91}} = 0.24$ (Boettcher, 2017). However, the albedo in urban areas is generally lower than in rural areas mainly due to pollution. Järvi et al. (2014) assessed and evaluated parameters in a snow scheme for two cold climate cities (Helsinki and Montreal) and suggested the parameters: $\alpha_{\mathrm{min,J14}} = 0.18$, $\tau_{\alpha,\mathrm{J14}} = 0.018$, and $\tau_{\mathrm{f},\alpha,\mathrm{J14}} = 0.11$. Both Verseghy (1991) and Järvi et al. (2014) assume a maximum snow albedo of 0.85. In Fig. 2, the decreasing albedo as described with Eqs. (35) (blue lines) and (36) (black lines) is shown for the parameters used in METRAS after Verseghy (1991) (solid lines) and the parameters based on Järvi et al. (2014) in MITRAS (dashed lines). According to Järvi et al. (2014), their suggested parameters fit well with observations in an urban area, which is why their parameters were chosen for MITRAS as well.

5 Consideration of cloud microphysics in MITRAS

The aim of extending the cloud microphysics parameterisation in MITRAS is to enable the analysis of the influence of an urban area on precipitation. Due to the very short time steps needed for numerical stability (well below 1 second) in microscale
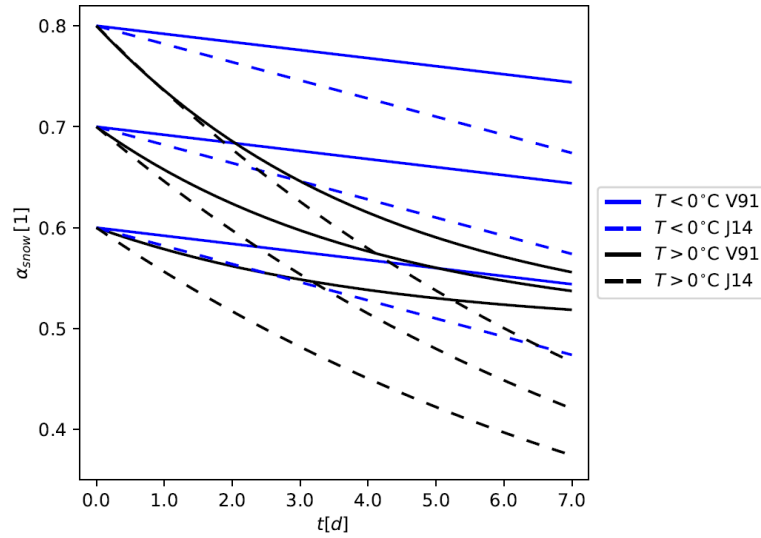
Figure 2. Linear (blue) and exponential (black) decrease of albedo of snow pack α_{snow} (Eqs. 35-36) as applied in METRAS ($\alpha_{\min} = 0.5$, $\tau_{\text{f},\alpha} = 0.24$, $\Delta t = 5$s) after Verseghy (1991) (V91, solid lines) and as applied in MITRAS ($\alpha_{\min} = 0.18$, $\tau_{\text{f},\alpha} = 0.11$, $\Delta t = 0.1$s) after Järvi et al. (2014) (J14, dashed lines).

models, explicitly resolving sedimentation is necessary. This also means, that processes like accretion and sedimentation have to be taken into account during the time step calculation. The representation of a winter precipitation event is significantly

300 improved by including an ice phase in the parameterisation. Consequently, all state-of-the-art bulk parameterisations include ice processes (Khain et al., 2015). However, currently the purpose of MITRAS is not to realistically represent the processes forming a precipitating cloud, since domain sizes are small (1 to 5 km) and thus a full formation of a cloud can only be simulated for zero wind situations and small clouds. Therefore, extending MITRAS with a comparably simple one-category ice scheme as described in Doms et al. (2011) is sufficient. There, no cloud ice is defined, but it is assumed that any cloud ice

305 is immediately transformed to snow particles (snow $q_1^{3\text{s}}$). The ice scheme processes are shown in blue in Fig. 3.

    The processes of the three-category warm rain scheme used in the M-SYS model system (Schlünzen et al., 2018a; Köhler, 1990) are provided in Section 2.2 and shown in grey and black in Fig. 3. In the following, the treatment of rain on roofs for MITRAS v3.1 as well as the model extension enabling the simulation of mixed-phase clouds for MITRAS v3.3 is given.
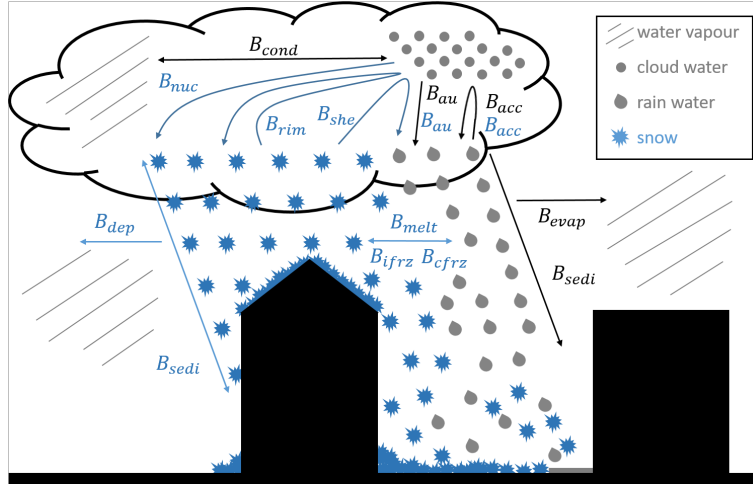
Figure 3. Cloud microphysics parameterisation with warm rain scheme in grey/ black and the one-category ice scheme in blue as introduced in MITRAS.

The following balance equations describe the microphysical processes in the extended cloud scheme:

$$\frac{\partial q_1^1}{\partial t} = - B_{\text{cond}} + B_{\text{evap}} - B_{\text{dep}} \tag{37}$$

$$\frac{\partial q_1^{2c}}{\partial t} = B_{\text{cond}} - B_{\text{au}}^{\text{c}} - B_{\text{nuc}} - B_{\text{acc}}^{\text{c}} - B_{\text{rim}} - B_{\text{she}} \tag{38}$$

$$\frac{\partial q_1^{2r}}{\partial t} = \frac{1}{\rho_0} \frac{\partial}{\partial z} \left(\rho_0 q_1^{2r} v_{\text{TR}} \right) + B_{\text{au}}^{\text{c}} + B_{\text{acc}}^{\text{c}} + B_{\text{she}} - B_{\text{evap}} + B_{\text{melt}} - B_{\text{ifrz}} - B_{\text{cfrz}} \tag{39}$$

$$\frac{\partial q_1^{3s}}{\partial t} = \frac{1}{\rho_0} \frac{\partial}{\partial z} \left(\rho_0 q_1^{2s} v_{\text{TS}} \right) + B_{\text{nuc}} + B_{\text{rim}} + B_{\text{dep}} - B_{\text{melt}} + B_{\text{ifrz}} + B_{\text{cfrz}} \tag{40}$$

$$\frac{\partial T}{\partial t} = \frac{L_{21}}{c_{\text{p}}} \left(\frac{p_{\text{S}}}{p_{\text{ref}}} \right)^{-\frac{R}{c_{\text{p}}}} \left(B_{\text{cond}} - B_{\text{evap}} \right) + \frac{L_{31}}{c_{\text{p}}} \left(\frac{p_{\text{S}}}{p_{\text{ref}}} \right)^{-\frac{R}{c_{\text{p}}}} B_{\text{dep}}$$

$$+ \frac{L_{32}}{c_{\text{p}}} \left(\frac{p_{\text{S}}}{p_{\text{ref}}} \right)^{-\frac{R}{c_{\text{p}}}} \left(B_{\text{nuc}} + B_{\text{rim}} - B_{\text{melt}} + B_{\text{ifrz}} + B_{\text{cfrz}} \right). \tag{41}$$

The balance equations are given for water vapour (Eq. 37), cloud water content (Eq. 38), rain water content (Eq. 39), snow water content (Eq. 40), and temperature (Eq. 41) with the latent heat of sublimation L_{31}, and the reference pressure $p_{\text{ref}} = 100\,000\,\text{Pa}$ following Doms et al. (2011). Prior to the model extensions, water vapour could condensate and cloud water evaporate (Eq. 9). In the sub-saturated air below the cloud, evaporation of rain (Eq. 11) occurs and in the now extended MITRAS deposition and sublimation of snow (B_{dep}) as well (Sect. 5.4). The coagulation of cloud drops produces rain (autoconversion, B_{au}^{c}) or snow (nucleation, B_{nuc}) (Sect. 5.2). The accretion of rain ($B_{\text{acc}}^{\text{c}}$), riming of snow ($B_{\text{rim}}$), and shedding ($B_{\text{she}}$) by melting snow particles collecting cloud droplets thereby producing rain is included (Sect. 5.3). The first terms on the right hand sides of Eqs. (39) and (40) represent sedimentation with the terminal velocities of rain (Eq. 5) and snow (v_{TS}, Sect.
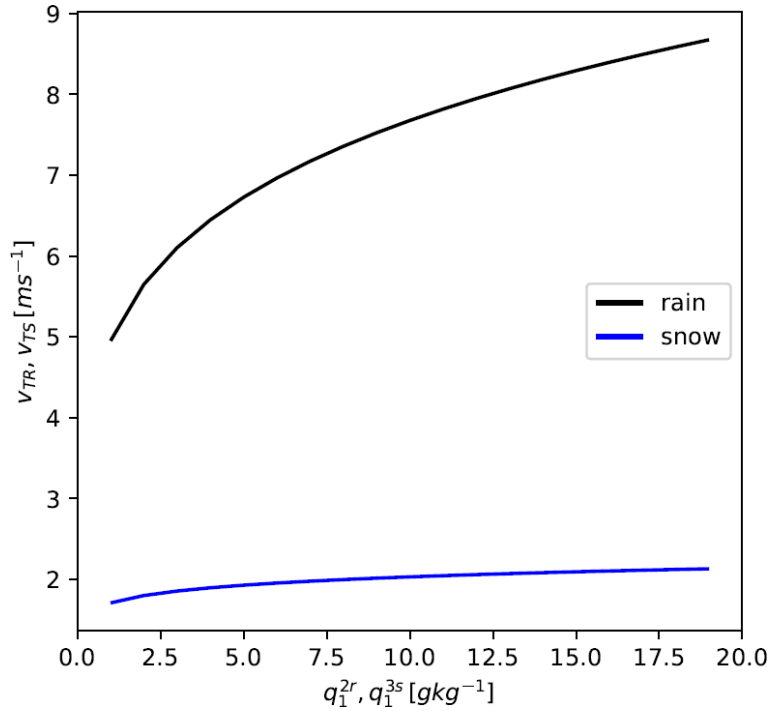
Figure 4. Terminal velocities of rain v_{TR} (black, Eq. 5) and of snow v_{TS} (blue, Eq. 42) as used in MITRAS.

5.1). Melting (B_{melt}) as well as immersion freezing (B_{ifrz}) and contact nucleation (B_{cfrz}) of snow are now considered (Sect.
5.5). For snowflakes the Gunn-Marshall size distribution (Gunn and Marshall, 1958) is assumed.

For the radiation parameterisation in MITRAS v4.0, snow is represented as spherical droplets like rain and is added to the liquid water content within the calculation of the absorption coefficient for the long wave radiation (Sect. 2.2).

5.1 Sedimentation

The terminal velocity for snow of

$$v_{\text{TS}} = 4.82\,\frac{\text{m}}{\text{s}} \left(\frac{\text{m}^3}{\text{kg}}\right)^{0.075} \cdot \left(10^{-3} \cdot \rho_0 \cdot q_1^{3s}\right)^{0.075} \tag{42}$$

(Doms et al., 2011) is introduced. Smaller densities at higher altitudes again need to be taken into account (compare with Eq. 6). The terminal velocity of snow is lower than that of rain with a maximum value of $2.2\,\text{ms}^{-1}$ (blue line in Fig. 4).

In general, precipitation rates and amounts are only given at ground surface in atmospheric models. In MITRAS, however, these precipitation quantities should be given on roofs as well. Precipitation quantities on roofs are calculated similar to the precipitation variables on ground (Ferner et al., 2022). For the sedimentation fluxes (first terms in Eqs. 39 and 40) in the atmosphere, the fluxes of rain and snow water content through the grid cell boundaries are calculated using the terminal

velocity defined at vector points and rain and snow water content defined at grid cell centres. For the precipitation quantities at ground, a terminal velocity for the scalar point just above ground is calculated. The precipitation quantities are then derived from the flux of rain and snow above surface. In case of a roof, the terminal velocity is calculated similarly, thus using the

340   scalar value of the terminal velocity just above the roof.

5.2   Autoconversion and nucleation

The development of snow from cloud water by subsequent diffusional growth is named nucleation. For the one-category ice scheme in MITRAS v3.3, a temperature dependence is considered:

$$
\epsilon(T) = \begin{cases} 0 & \text{if } T \geq T_0 \\ 0.5\left[1 + \sin\left(\frac{\pi \cdot (0.5(T_0 + T_2) - T)}{T_0 - T_2}\right)\right] & \text{if } T_2 < T < T_0 \\ 1 & \text{if } T \leq T_2. \end{cases} \tag{43}
$$

345   According to Doms et al. (2011), it is based on observations of the frequency distribution of water and ice in mixed-phase clouds. $\epsilon(T)$ is one below the minimum temperature $T_2 = 235.16\,\text{K}$ and zero above the freezing point (T_0). Note, that the conversion coefficient for Kelvin in MITRAS is 273.16 and not 273.15 as in (Doms et al., 2011).

    The conversion rates are given as

$$
B_{\text{au}}^{\text{c}} = \max(0, k_{\text{cold}}^{\text{r}} \cdot (1 - \epsilon(T)) \cdot \left(q_1^{2\text{c}} - q_{1,\text{cri}}^{2\text{c}}\right) \tag{44}
$$

350   $$
B_{\text{nuc}} = \max(0, k_{\text{cold}}^{\text{s}} \cdot \epsilon(T) \cdot \left(q_1^{2\text{c}} - q_{1,\text{cri}}^{2\text{c}}\right) \tag{45}
$$

with the autoconversion interval for rain $k_{\text{cold}}^{\text{r}} = 10^{-4}\,\text{s}^{-1}$ and for snow $k_{\text{cold}}^{\text{s}} = 10^{-3}\,\text{s}^{-1}$ (Doms et al., 2011). Note, that unlike in Doms et al. (2011), a nonzero value for $q_{1,\text{cri}}^{2\text{c}}$ is chosen in MITRAS.

    In Fig. 5 the autoconversion rates for warm clouds (Eq. 7, red) and mixed phase clouds (Eq. 44, blue) are shown as well as the nucleation rates (Eq. 45, black). All processes increase with increasing cloud water contents. While the autoconversion

355   in the warm rain scheme only depends on the cloud water content, the other processes additionally depend on temperature. When mixed-phase clouds are assumed, less rain water is created by autoconversion than in warm clouds for the same cloud water content. Below $T_2 = 235.16\,\text{K}$ the nucleation of snow is highest and the autoconversion is zero. The nucleation gradually decreases and the autoconversion increases with higher temperatures until the freezing point is reached.

5.3   Accretion and riming

360   For riming, the continuous model for particle growth by collection is applied. Snow particles have no spherical shapes. Instead, they are assumed to be rimed aggregates of crystals and they have the form of thin circular plates. The temperature dependent mass-size relation of snow is defined as

Figure 5. Autoconversion rates for warm clouds (red, $B_{\mathrm{au}}^{\mathrm{w}}$, Eq. 7) and mixed phase clouds (blue, $B_{\mathrm{au}}^{\mathrm{c}}$, Eq. 44) and nucleation rates (black, B_{nuc}, Eq. 45) for different cloud water contents $q_1^{2\mathrm{c}}$ and temperatures T.

$$a_{\mathrm{m}}(T) = \begin{cases} a_{\mathrm{mc}} - a_{\mathrm{mv}} \left[1 + \cos\left\{ \frac{2\pi(T - 0.5(T_0 + T_1))}{(T_0 - T_1)} \right\} \right] & \text{if } T_0 > T > T_1 \\ a_{\mathrm{mc}} & \text{else} \end{cases} \tag{46}$$
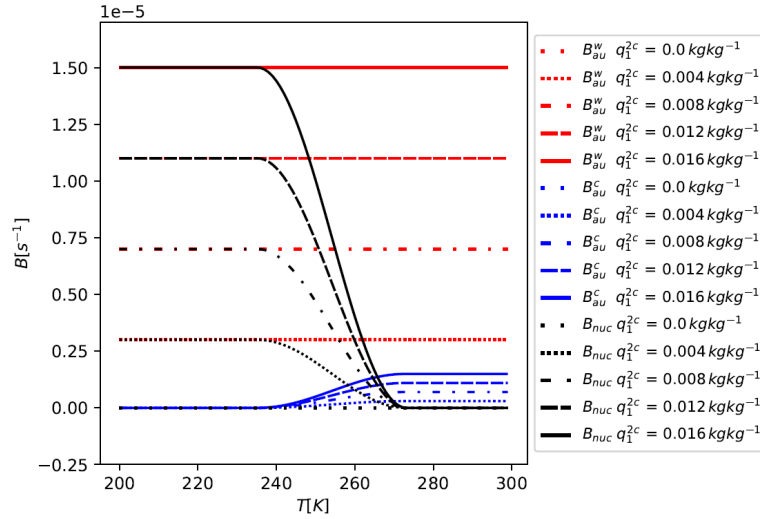
with the constant parameters $a_{\mathrm{mc}} = 0.08\,\mathrm{kg\,m^{-2}}$ and $a_{\mathrm{mv}} = 0.02\,\mathrm{kg\,m^{-2}}$ and the temperature $T_1 = 253.16\,\mathrm{K}$ (Doms et al., 2011).

For the accretion term (Eq. 8) in the one-category ice scheme, the temperature dependency (Eq. 43) is considered:

$$B_{\mathrm{acc}}^{\mathrm{c}} = (1 - \epsilon(T)) \cdot \frac{934.63}{\mathrm{s}} \left(\frac{\mathrm{m}^3}{\mathrm{kg}} \right)^{0.875} \cdot q_1^{2\mathrm{c}} \cdot \left(\rho_0 \cdot 10^{-3} \cdot q_1^{2\mathrm{r}} \right)^{0.875} \tag{47}$$

$$B_{\mathrm{rim,MITRAS}} = \begin{cases} \frac{1}{a_{\mathrm{m}}(T)} \cdot 3307.24\,\frac{\mathrm{kg}}{\mathrm{s\,m^2}} \left(\frac{\mathrm{kg}}{\mathrm{m}^3} \right)^{-1.075} \cdot q_1^{2\mathrm{c}} \cdot \left(\rho_0 \cdot 10^{-3} \cdot q_1^{3\mathrm{s}} \right)^{1.075} & \text{if } T < T_0 \\ 0 & \text{if } T \geq T_0. \end{cases} \tag{48}$$

Otherwise it remains the same as in MITRAS v3.0. Note, that (Doms et al., 2011) uses different parameters for the accretion.

In Fig. 6, the accretion rates for the warm rain parameterisation used in MITRAS v3.0 (grey) and the mixed-phase cloud parameterisation as used in MITRAS v4.0 (light blue) is shown as well as the riming rates (dark blue). Accretion increases for rain for temperatures above T_2 (Eq. 43) reaching the same value as warm clouds at the freezing point T_0. The riming rate is highest at $-10\,°\mathrm{C}$, as the largest snowflakes can be found at $-10\,°\mathrm{C}$ (Eq. 46). Snow production is higher than rain production for the same initial snow respectively rain amount.
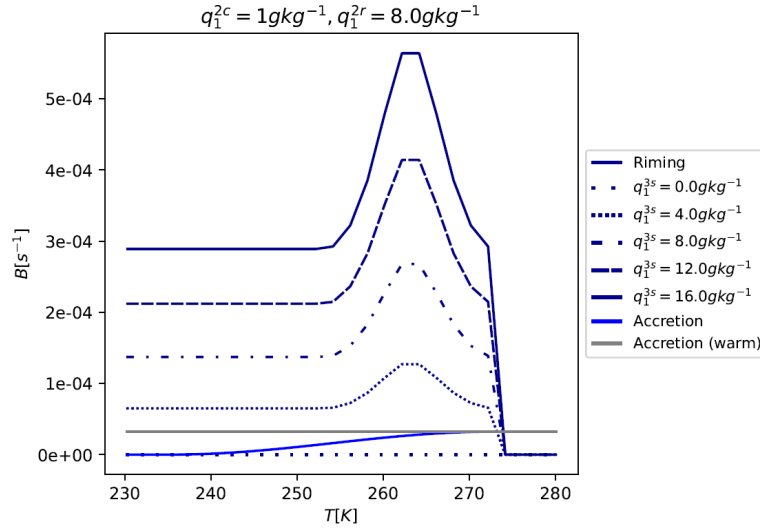
Figure 6. The riming rates (Eq. 48, dark blue) with the cloud water content of $q_1^{2c} = 1 \cdot 10^{-3}\,\mathrm{kg\,kg^{-1}}$ for various snow water contents q_1^{3s} depending on the temperature T and the accretion rates for $q_1^{2c} = 1 \cdot 10^{-3}\,\mathrm{kg\,kg^{-1}}$ and the rain water content $q_1^{2r} = 8 \cdot 10^{-3}\,\mathrm{kg\,kg^{-1}}$ for the mixed-phased cloud parameterisation as used in MITRAS v3.3 (Eq. 47, light blue) and warm cloud parameterisation as used in MITRAS v3.0 (Eq. 8, grey).

At temperatures below the freezing point T_0, snow is produced by riming. If it is warmer, rain water content is produced by shedding. The equation is the same as riming (Eq. 48), but it produces rain water and not snow.

5.4 Depositional growth

With the inclusion of snow, depositional growth (diffusion growth of snow particles) and sublimation occur, which is according
380 to Doms et al. (2011) given as

$$B_{\mathrm{dep}} = \frac{\alpha_{\mathrm{dep}}}{(a_{\mathrm{m}}(T))^{0.5}} \left(1 + \frac{\beta_{\mathrm{dep}}}{(a_{\mathrm{m}}(T))^{0.25}} \left(\rho_0 q_1^{3\mathrm{s}}\right)^{0.225}\right) \left(q_1^1 - q_{1,\mathrm{sat,ice}}^1\right) \left(\rho_0 q_1^{3\mathrm{s}}\right)^{0.625} \tag{49}$$

with the factors

$$\alpha_{\mathrm{dep}} = \left(1.09 \cdot 10^{-3} - 3.34 \cdot 10^{-5} \left(T - T_0\right)\right) \tag{50}$$

and $\beta_{\mathrm{dep}} = 13.0$. $q_{1,\mathrm{sat,ice}}^1$ denotes the saturation specific humidity over ice. For better readability, the units of α_{dep} and β_{dep}
385 are not provided here. They can be found in Doms et al. (2011).

5.5 Melting and freezing

The melting rate is derived similarly to the evaporation and deposition rates leading to

$$B_{\mathrm{melt}} = \frac{\alpha_{\mathrm{melt}}}{a_{\mathrm{mc}}^{0.5}} \left(1 + \beta_{\mathrm{melt}} a_{\mathrm{mc}}^{0.25} \left(\rho_0 q_1^{3\mathrm{s}}\right)^{0.225}\right) (T - T_0) \left(\rho_0 q_1^{3\mathrm{s}}\right)^{0.625} \tag{51}$$

with the factors $\alpha_{\mathrm{melt}} = 7.2 \cdot 10^{-6}$ and $\beta_{\mathrm{melt}} = 13.0$ (Doms et al., 2011).

Rain drops can be activated as ice nuclei due to various drop impurities (immersion freezing), this is represented in the model as

$$B_{\mathrm{ifrz}} = \alpha_{\mathrm{if}} \left(e^{\alpha_{\mathrm{if}}(T_0 - T)} - 1\right) \left(\rho_0 q_1^{2\mathrm{r}}\right)^{1.75} \tag{52}$$

with the parameter $\alpha_{\mathrm{if}} = 9.95 \cdot 10^{-5}$ (Doms et al., 2011).

The process of falling rain drops collecting ice nuclei (contact freezing nucleation) is represented as

$$B_{\mathrm{cfrz}} = \begin{cases} \alpha_{\mathrm{cf}} E_{\mathrm{cf}} N_{\mathrm{cf},0} (270.17 - T)^{1.3} (\rho_0 q_1^{2\mathrm{r}})^{1.625} & \text{if } T < 270.17\,\mathrm{K} \\ 0 & \text{if } T \geq 270.17\,\mathrm{K} \end{cases} \tag{53}$$

with the parameter $\alpha_{\mathrm{cf}} = 1.55 \cdot 10^{-3}$, the collection efficiency $E_{\mathrm{cf}} = 5.0 \cdot 10^{-3}$, and the concentration of natural contact ice nuclei active at $-4°\mathrm{C}$ at sea level $N_{\mathrm{cf},0} = 2.0 \cdot 10^5$ (Doms et al., 2011). Again, the units can be found in Doms et al. (2011).

6 Validation

Previous versions of MITRAS are confirmed to represent well the main atmospheric features within an urban boundary layer. MITRAS v1.0 has been validated in comparison to wind tunnel data (Schlünzen et al., 2003; Grawe et al., 2013). MITRAS v2.0 (Salim et al., 2018) has been evaluated using the VDI guideline for microscale, obstacle-resolving models (Grawe et al., 2015). The model extensions concerning radiation in MITRAS v3.0 are described and validated in Fischereit (2018). As most parts of the extended model are already validated (e.g. Ferner et al., 2022), an assessment of the plausibility of the model results is performed here. Furthermore, tests in comparison to measured data are challenging, because in a model domain of this size hardly any high-resolution in-situ data are available.

For a more in depth assessment of the winter parameterisations introduced in the current paper, model results achieved by using different model versions are compared using "to be expected outcomes" for an assessment. The set-ups of the simulations and corresponding model version number are listed in Tab. 1. MITRAS v3.0 is considered to be the initial version (index "init" in name). MITRAS v3.1 (index "wr") includes neglecting the influence of terrain steepness on horizontal diffusion terms (Sect. 3.1), changing the structure of all scalar obstacle surface variables and introduction of boundary conditions at obstacle surfaces for water content variables (Sect. 3.2), and sedimentation of rain on roofs (Sect. 5.1). In a previous study, MITRAS v3.1 has been tested with focus on the reliability of the rain processes in comparison with in-situ rain radar data (Ferner et al., 2022). MITRAS v3.3 includes the winter precipitation scheme (use denoted by index "ice" in Table 1) described in Sects. 4 and 5.

Table 1. Set-up for simulations with different initial surface temperatures T (W for warm, C for cold, H for hot), cloud water contents q_1^{2c}, and development stage of the model. For details see text.

Name	T [K]	q_1^{2c}	version	extensions included	comment
Winit	280	none	3.0		
Wwr	280	profile	3.1	Horizontal diffusion terrain steepness neglected; changed array structure; water contents at building surfaces; sedimentation on roofs	no parallelisation no precipitation
Wwr_np	280	profile	3.1		
Wwr_noprecip	280	none	3.1		
Cwr	272	profile	3.1		
Hwr	288	profile	3.1		
Cice	272	profile	3.3	v3.1; snow cover; one-category ice scheme	
Wice	280	profile	3.3		
Hice	288	profile	3.3		

6.1 Model set-up

415 All simulations are performed for the same model domain (Sect. 6.2). For the plausibility tests in Sect. 6.4, simulations with three different initial surface level temperatures ("C" for cold, "W" for warm, "H" for hot in Tab. 1) are performed. In Fig. 7, the initial temperature profiles are provided in black. For the profile, a potential temperature gradient of $0.001\,\mathrm{K\,m^{-1}}$ is assumed. For all simulations except Winit and Wwr_noprecip, nonzero initial cloud water contents (blue solid line in Fig. 7) are prescribed which lead to heavy precipitation. The initial surface level pressure is $990\,\mathrm{hPa}$, the initial wind at $150\,\mathrm{m}$ above

420 ground is from west ($2\,\mathrm{m\,s^{-1}}$). Due to Coriolis force effects, the wind direction at $10\,\mathrm{m}$ height is south west with a friction reduced wind speed of $1.2\,\mathrm{m\,s^{-1}}$. The initial relative humidity is set to $60\,\%$ at ground and reduces to $30\,\%$ at the top of the model domain ($5\,\mathrm{km}$) yielding the specific humidity profiles in Fig. 7 (dash-dotted, dashed, dotted blue lines).

The plausibility tests are performed using hit rates (Sect. 6.3). To determine them, allowed uncertainty ranges have to be found for the meteorological variables. This is based on published methods to asses obstacle-resolving model performance and

425 is done for variables by comparing model results with and without parallelisation (Wwr and Wwr_np in Tab. 1).

6.2 Model domain

The model domain is small to ensure a fast integration. However, it includes orography, slanted roofs, obstacle corners and different surface cover classes to assess, if the model can represent the different features for a realistic urban area. The domain extends $240\,\mathrm{m} \times 210\,\mathrm{m}$ horizontally and $6400\,\mathrm{m}$ vertically with an equidistant area of $3\,\mathrm{m}$ resolution in the middle (Fig. 8). The

430 grid increases towards the lateral boundaries to a maximum horizontal resolution of $10\,\mathrm{m}$. The maximum vertical resolution of $500\,\mathrm{m}$ is achieved at $3\,\mathrm{km}$ above ground. Typically, domains of obstacle-resolving models extend only few hundred metres vertically (Geletič et al., 2022; Grawe et al., 2013). However, with interest in cloud and precipitation development in the
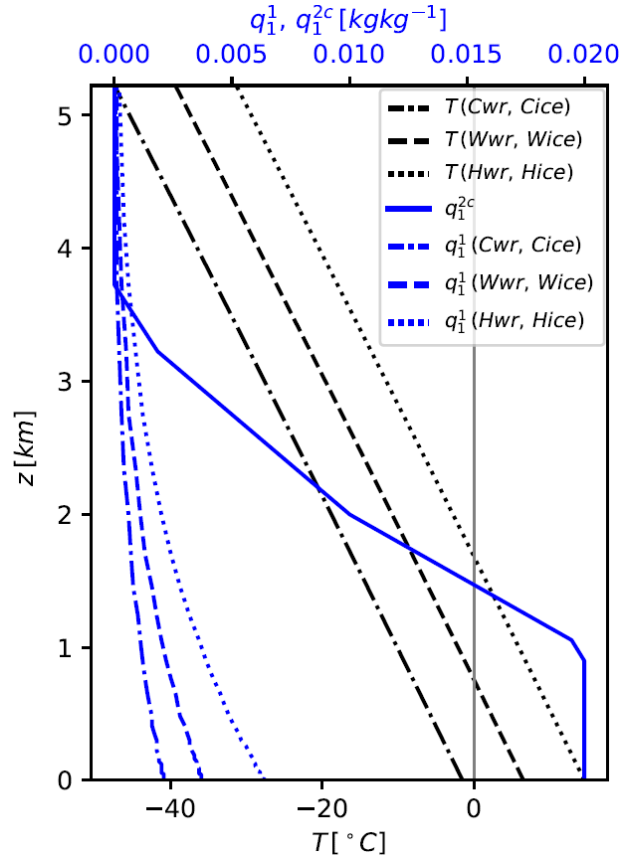
Figure 7. Initial temperature (black), specific humidity q_1^1 and cloud water content q_1^{2c} (both blue) vertical profiles for cold (dashdotted line), warm (dashed line), and hot cases (dotted line). The cloud water content profile (solid line) is identical for all cases that include precipitation. The grey line denotes the freezing point.

influence of a building, the upper level is chosen high enough to ensure a vertical extension of clouds is not hindered by a too low model top. Grid sizes increase in horizontal as well as vertical direction by a factor of 1.175. The equidistant area ranges

435   from $-28\,\text{m}$ to $26\,\text{m}$ in the x-direction and -16 to $18\,\text{m}$ in the y-direction and from the ground up to $32\,\text{m}$.

A single building with roof heights at $15\,\text{m}$ and $10\,\text{m}$, and a size of $45\,\text{m}$ by $45\,\text{m}$ (Fig. 9) including edges and slanted surfaces is placed on top a small mound. This setup resembles a terp, which is a North European form of housing, where an artificial mound protects the building from flooding. At the boundaries is cropland. The pavement and the streets are made of asphalt. At obstacles, the surface cover class is concrete (Fig. 10).

440   The simulations start for 7:30 and finish for 8:32. Within this time span, a precipitation event takes place and the sun rises. The focus area of the analyses lies in the centre of the domain (dashed lines in Figs. 8 and 10).
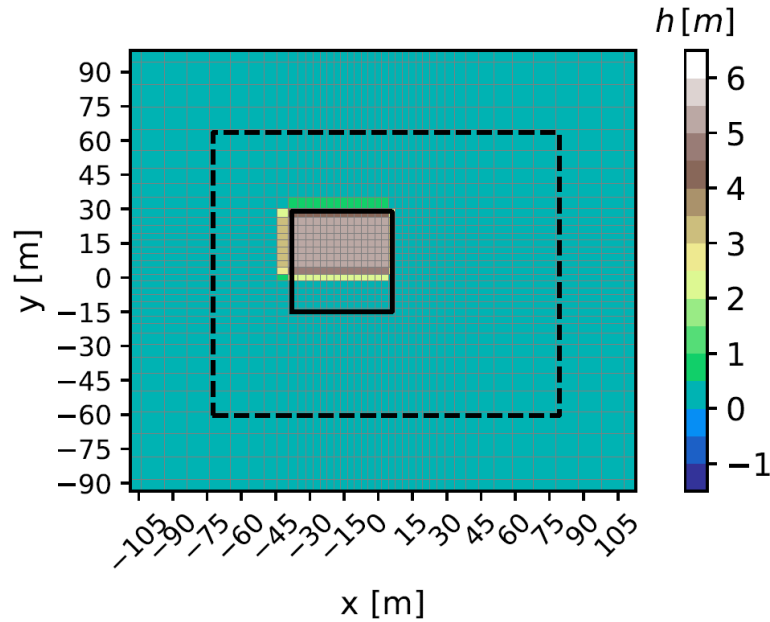
Figure 8. Orography height h (shaded) of model domain. The solid line denotes the contour of the building and the black dashed line the model domain taken into account in the result analyses. Thin lines illustrate the horizontal grid.
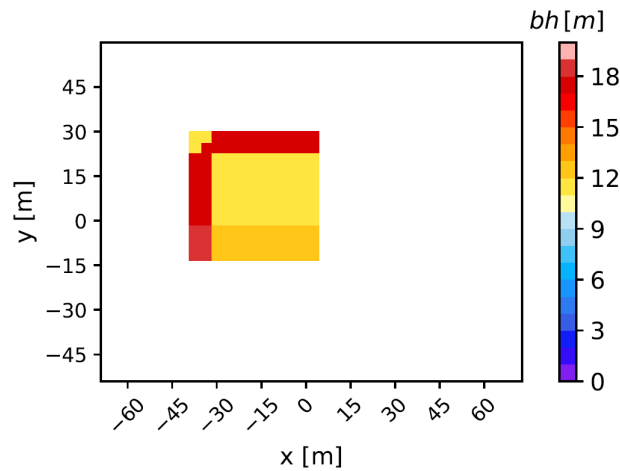
Figure 9. Roof height bh.

6.3   Derivation of model uncertainty values

The assessment, whether model results are identical or different is based on a method described in VDI (2017) which uses hit rates. Hit rates have been applied in the past for assessing microscale models (e.g. Eichhorn and Kniffka, 2010; Franke et al.,
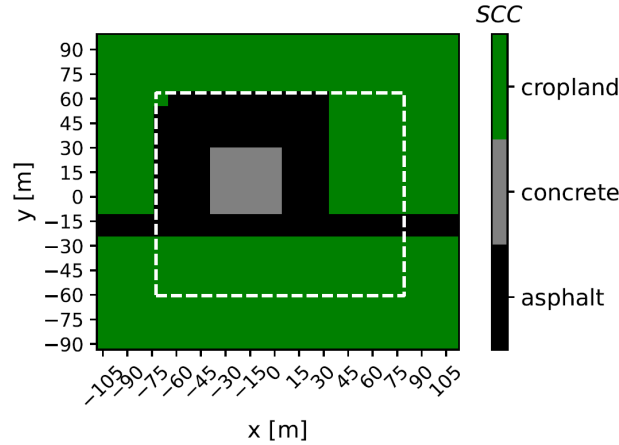
Figure 10. Surface cover classes. The dashed line denotes the model domain taken into account in the result analyses.

Table 2. Thresholds for the absolute (W) and relative deviation (D) for hit rate calculation (q) for wind speed components u, v, w, temperature T, net long and short wave radiation LW_net and SW_net, and precipitation amount P on ground. For details on their derivation see text.

	u	v	w	T	LW_net	SW_net	P
W	$0.02\,\text{ms}^{-1}$	$0.02\,\text{ms}^{-1}$	$0.02\,\text{ms}^{-1}$	$0.05\,\text{K}$	$0.5\,\text{Wm}^{-2}$	$0.5\,\text{Wm}^{-2}$	$0.001\,\text{mm}$
D [%]	5	5	5	0.02	0.5	0.2	1

445   2012; Grawe et al., 2013). as well as for other model scales (e.g. weather forecast (Cox et al., 1998), mesoscale air quality and meteorology models (Schlünzen and Sokhi, 2008)). The hit rate q is defined as:

$$q = \frac{1}{N} \sum_{i=1}^{N} n_i \tag{54}$$

with N being the total number of compared values and n_i equal 1 (hit) or 0 (fail) depending on the deviation of model results and comparison data:

450    $$n_i = \begin{cases} 1 & \text{if } \left| \frac{Pd_i - O_i}{O_i} \right| \leq D \text{ or } |Pd_i - O_i| \leq W \\ 0 & \text{else.} \end{cases} \tag{55}$$

For every atmospheric grid cell at location i, the wind speed is assessed per component (u, v, w). The comparison results in a hit ($n_i = 1$), if the relative deviation does not exceed the threshold value, D, or the absolute deviation remains below the corresponding threshold W. When comparing model results to observational data, Pd_i denotes the predicted and O_i the observed values. In the present study, results of different model versions are compared. Pd_i denotes the newer model version

455 and O_i the older version. Following VDI (2017) and WMO (2023), a hit rate of $q \geq 95\%$ between two simulation results are considered similar. There, the threshold values for absolute and relative deviations, W and D, for the wind speed components speeds are $W_{\mathrm{VDI}} = 0.01\,\mathrm{m\,s^{-1}}$ and $D_{\mathrm{VDI}} = 0.05$. Wind speed components are normalised with the reference wind speed U_{ref} for the test cases. In the current study, the initial wind speed of $2\,\mathrm{m\,s^{-1}}$ is used as reference wind speed. As non-normalised values are compared, W has to be adjusted to $W = W_{\mathrm{VDI}} \cdot U_{\mathrm{ref}} = 0.02\,\mathrm{m\,s^{-1}}$ (Tab. 2). For the relative deviation, D_{VDI} is

460 assumed for D for each of the wind speed components (Tab. 2). It should be noted that these values are about a factor of 10 smaller than the required measurement uncertainties for wind speed given in WMO (2023).

In this study, not only the results for the components of the wind vector but also the results for temperature, long and short wave radiation, and precipitation amount on ground P are assessed. The W and D values for these meteorological variables are derived by comparing the results of MITRAS v3.0 with one running in parallel processing mode and the other one with single

465 processor use (with and without parallelisation; Wwr and Wwr_np) after one hour of simulation. This measure is taken, since the same model might yield different results depending on compilers, installed packages, and hardware. Therefore, hit rates below 100% can occur (e.g. 98% for v, Tab. 3). As a hit rate above 95% means the results lie within the required accuracy, Wwr and Wwr_np can be considered identical (Tab. 3).

With computational accuracy a strict criterion is applied for temperature, radiation, and precipitation. The resulting W and

470 D values are consistent with the allowed uncertainty values for the wind speed components, as they also are about a factor of 10 smaller than given in WMO (2023). For example, the achievable uncertainty for temperature suggested by WMO (2023) is $0.2\,\mathrm{K}$ and here $0.05\,\mathrm{K}$ is chosen. For long and short wave radiation $1/10^{\mathrm{th}}$ of the values for direct solar radiation ($4 - 6\,\mathrm{W\,m^{-2}}$ WMO, 2023) is used. The allowed absolute deviation of $0.001\,\mathrm{mm}$ for precipitation is well below the accuracy of commonly used rain gauges ($0.1\,\mathrm{mm}$, WMO, 2023). This strict value is chosen because precipitation is the target value of our model

475 extensions. Low hit rates give the impression of larger differences. It should be noted that the dependency of the hit rate on the allowed deviations is a shortcoming of this validation metric as discussed in Franke et al. (2012). On the other hand, the comparison of results of different model versions should lead to very similar results (e.g. with/ without parallelisation, code extensions used with values of zero for the variables), while extensions of a model with new or changed process descriptions should provide different model results.

480 **6.4 Model plausibility and functionality**

6.4.1 Influences of the modifications of the diffusion

The comparison of the results from simulations using MITRAS v3.1 (Wwr_noprecip) with simulations using MITRAS v3.0 (Winit) for dry atmospheric conditions would show any influences of changes due to the calculation of the horizontal diffusion of scalars (Sect. 3.1) and the modified structure for all scalar quantities at obstacle surfaces (Sect. 3.2). The changes of the

485 model physics by the modifications in horizontal diffusion are small, but due to the strictness of the required accuracy, a good agreement with hit rates of 95% is not expected for the whole domain. As the effects of slopes are largest close to the ground surface, the largest discrepancies are to be expected there. Not surprisingly, hit rates are below 95% for the wind speed

Table 3. Hit rates q in percent of wind components (u, v, w), temperature (T), net surface long wave and short wave radiation (LW_{net} SW_{net}), and precipitation amount (P) on ground after 1 hour simulation time.

Cases	u	v	w	T	LW_{net}	SW_{net}	P
Wwr - Wwr_np	100	98	100	100	100	100	100
Wwr_noprecip - Winit	93	84	92	95	100	100	-
Wwr - Wwr_noprecip	28	3	40	0	0	0	0
Cice - Cwr	39	9	34	5	3	0	100
Hice - Hwr	9	4	27	4	0	0	48
Wice - Wwr	39	6	37	4	0	0	60

components (Tab. 3). The results for temperature, long and short wave radiation can be considered identical. The lowest hit rate in this comparison of $84\,\%$ is found for the lateral wind component v. Misses are only found in grid cells near the ground (Fig. 11), where the terrain steepness of the terrain-following coordinate system has the most effect, which is plausible.
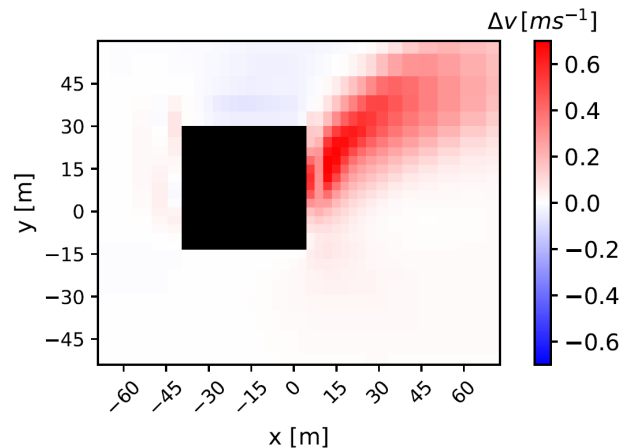
Figure 11. Difference of v-wind component Δv of Wwr_noprecip and Winit at $1.5\,\mathrm{m}$ height.

6.4.2 Influences of cloud formation

The influence of the presence of atmospheric liquid water on the radiation is included in MITRAS v3.1. When liquid water is present, shading by clouds is considered using the two-stream approach instead of the vertically integrated radiation approach (Sect. 2.2). This leads to different net surface radiations. Comparing simulations with and without precipitation (Wwr and Wwr_noprecip) therefore reveals, not surprisingly, profound differences with hit rates below $40\,\%$ for all meteorological variables with the flow field being more similar than the temperature, short and long wave radiation and precipitation (Tab.

3). Without precipitation, the shadow cast by the building and the reflection by the small elevation can be seen very clearly in the net surface short wave radiation (not shown). This effect is not as pronounced when cloud water is present as the cloud blocks the radiation. However, the differences still show the direct shading by building and slope (Fig. 12). With and without liquid water, the net surface long wave radiation is negative meaning the net flux is outward. However, the absolute values are larger without liquid water in the atmosphere (not shown) as there is less backscattering and surfaces get warmer. These results confirm Ferner et al. (2022), where results of MITRAS v3.1 were compared with in-situ measurements and the model has been shown to produce plausible results.
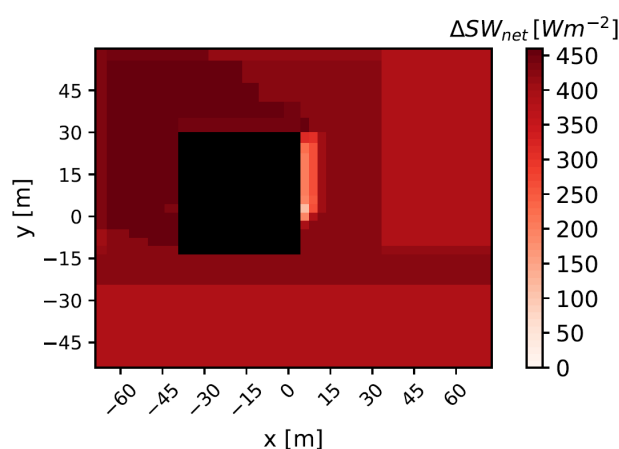
Figure 12. Difference of net surface short wave radiation ΔSW_{net} of Wwr and Wwr_noprecip.

6.4.3 Influences of snow cover

By including snow cover (Sect. 4) in MITRAS v3.3, the homogenising effect of snow cover on the albedo is represented in the model. The snow cover parameterisation is implemented in Cice and the temperature is sufficiently low for snow to reach the ground and remain. Without snow cover, most of the focus area is asphalt (Fig. 10) with an albedo of 0.09. Cropland has an albedo of 0.2. Without snow cover (case Cwr), the median of the albedo therefore is 0.09. This can be seen in Fig. 13, where box plots of albedo values of cases Cice (grey, MITRAS v3.3) and Cwr (blue, MITRAS v3.1) are shown. For Cwr, the box plots remain the same over time. With snow cover (Case Cice), the median increases with increasing snow cover, while the spread of the albedo data decreases. The albedo does not reach the maximal snow albedo of 0.85 (Sect. 4.5), meaning that underlying soil still slightly shines through.

6.4.4 Influence of temperature on precipitation

The cloud microphysics parameterisation in MITRAS v3.1, which does not include snow (Cwr, Wwr, Hwr), as well as the one-category ice scheme applied in MITRAS v3.3 (Cice, Wice, Hice) are mass conserving. Therefore, the precipitation amounts on ground are expected to be similar after one hour of simulation, as they depend only on the temperature and not on the
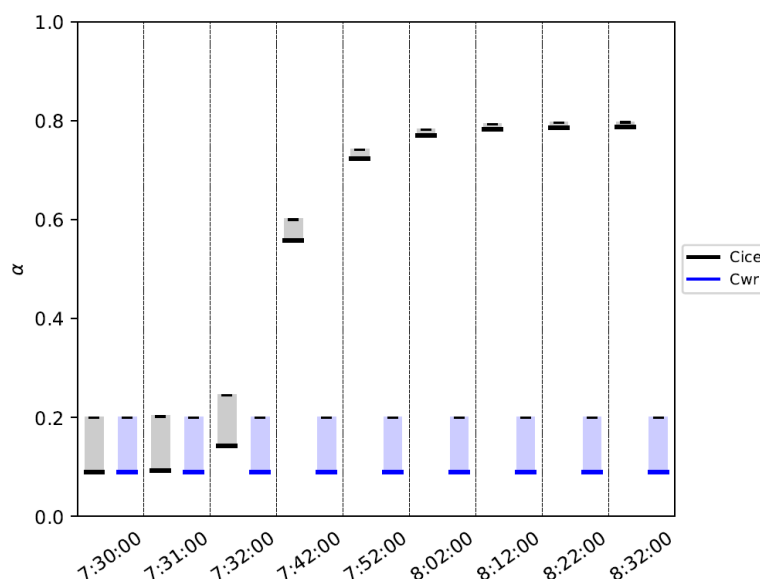
Figure 13. Box plots of albedo α for Cice (dark blue) and Cwr (light blue) show the median and the quartiles. The lower thick line denotes the median while the box represents the quartiles.

used model version (Tab. 3, hit rate for P 100 % for compared cases Cice and Cwr). For the other meteorological variables, more disagreement with hit rates below 95 % is expected due to the strictness of the required accuracy. Especially for radiation and temperature profound differences are found (Tab. 3, hit rates below 5 %). The wind field retains some common features

520 (hit rates up to 39 %). In Fig. 14, the spatial mean precipitation amounts on ground over time are presented for rain (dashed lines), snow (dotted lines), and rain + snow (solid lines). As there is no snow in MITRAS v3.1 (Cwr, Wwr, Hwr), the complete precipitation amount is given in dashed lines for these cases, as it equals the rain amount. After half an hour of simulations, the precipitation curves have converged. However, the hit rates of the precipitation amount for the comparisons of MITRAS v3.3 and v3.1 for "hot" (288 K at surface, Hice and Hwr) and warm (280 K at surface, Wice and Wwr) are below 95 %

525 (Tab. 3), meaning, the results do not lie within the required accuracy. When allowing less strict required accuracies based on observational uncertainties following WMO (2023) ($W = 0.1$ mm, $D = 5$ %), the comparison of precipitation of the different model versions yield hit rates of 100 %. This further underlines the sensitivity of the hit rate to the choice of allowed deviation.

The higher the temperature, the more water vapour the atmosphere can carry before saturation is reached resulting in less precipitation amounts. This is well represented in the model (MITRAS v3.1 and MITRAS v3.3). The final precipitation amounts

530 are smaller for higher temperatures (from black and blue lines over yellow to red curves in Fig. 14). More of rain and snow water content evaporates or sublimates in the sub-saturated areas below the cloud than it would in colder cases. Simultaneously, the production of cloud water content by condensation is reduced. In this study, water vapour is prescribed using the relative humidity leading to temperature dependent specific humidity profiles (Fig. 7). This does not represent that more precipitation is expected in a warming climate (e.g. Purr et al., 2021).
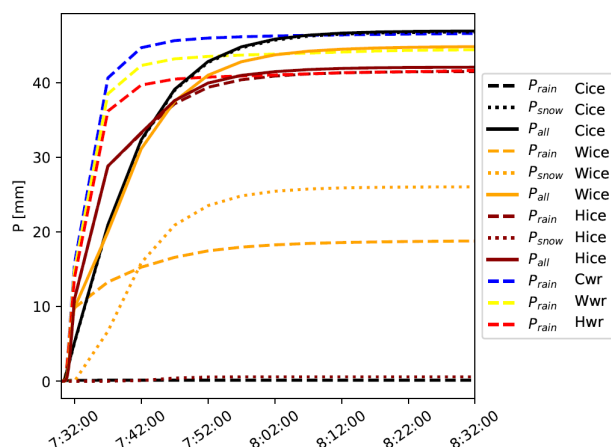
Figure 14. Precipitation amounts on ground for Cice (black), Wice (orange), Hice (brown), Cwr (blue), Wwr (yellow), and Hwr (red). Rain is given in dashed lines, snow in dotted lines and rain and snow together are given as solid lines.

6.4.5 Influence of one-category ice scheme

The level of detail is increased in MITRAS v3.3 by extending the model with a one-category ice scheme (Sect. 5) improving the representation of precipitation in winter. During the first minutes of the simulation, the amount of precipitation on ground increases faster with time if only warm precipitation is considered (MITRAS v3.1, dashed lines in Fig. 14) than when also considering the ice phase (MITRAS v3.3, solid lines). In the warm rain Kessler-scheme, the sedimentation of small rain drops is overestimated leading to the calculation of too much precipitation during the process of rain formation (Schlünzen et al., 2018a). This effect is reduced with the one-category ice scheme parameterisation, because precipitation develops slower with this new parameterisation. These changes have consequences on radiation, temperature and wind field, which explains the low hit rates (Tab. 3).

7 Summary and Conclusions

The microscale and obstacle-resolving model MITRAS was extended by modifying the diffusion of scalars (Sect. 3.1) as well as including boundary conditions for cloud and rain water content at obstacle surfaces (Sect. 3.2) and a snow cover scheme (Sect. 4). The cloud microphysics scheme for warm clouds was extended with a one-category ice scheme (Sect. 5). This makes MITRAS the first obstacle-resolving atmospheric model that includes precipitating snow.

Previous model versions of MITRAS are confirmed to represent well the main features of an urban boundary layer (Schlünzen et al., 2003; Grawe et al., 2013, 2015; Fischereit, 2018). The performance of the warm rain scheme and the newly introduced boundary conditions (v3.1) has been validated by Ferner et al. (2022). The parameterisations for snow cover and the one-category ice scheme have already been applied in mesoscale models (Boettcher, 2017; Doms et al., 2011). The modifications of the parameterisations for the characteristics of a microscale and obstacle-resolving model are validated here by testing for

plausibility (Sect. 6) by comparing model results of different model versions (v3.0, v3.1, v3.3). The model features presented
555 in this paper are included in MITRAS v4.0 as are features not relevant to this study (e.g. v3.2, Badeke et al., 2021).

For the plausibility tests, simulations were compared based on a procedure described in VDI (2017) for obstacle-resolving models, where hit rates are calculated for the wind speed components. In our study, additional hit rates for temperature, radiation, and precipitation were determined on the basis of computational accuracy. The resulting required deviations are $0.05\,\mathrm{K}$ ($0.02\,\%$) for temperature, $0.5\,\mathrm{Wm}^{-2}$ ($0.5\,\%$) for long wave radiation, $0.5\,\mathrm{Wm}^{-2}$ ($0.2\,\%$) for short wave radiation, and
560 $0.001\,\mathrm{mm}$ ($1\,\%$) for precipitation.

Comparisons of different model versions reveal that the model produces plausible results. Neglecting terrain-steepness in the diffusion calculation for scalars in MITRAS v3.1 and extending the cloud microphysics scheme in MITRAS v3.3 causes expected differences. The plausibility tests also reveal that taking precipitation into account in a microscale obstacle-resolving model is crucial due to the profound influence of clouds on radiation. Even though state-of-the-art bulk cloud microphysics
565 parameterisations are more complex than the one-category ice scheme applied in MITRAS (Khain et al., 2015), an improvement compared to the previously applied warm rain scheme (Köhler, 1990) has been shown. The overestimation of precipitation during the process of rain formation (Schlünzen et al., 2018a) is reduced. The homogenising effect of snow on the albedo is plausibly reproduced.

In order to increase the level of detail of MITRAS' winter parameterisation, the effects of snow on the roof's albedo or
570 roughness length should be considered. Moreover, the effects of different isolation properties of buildings should be included for instance to study anthropogenic heat emissions on warming and snow melting as well as on the indoor building temperature. For the analyses of frost heterogeneities e.g. on roads and walkways, the inclusion of freezing rain or refreezing snow would be useful, even though it is already possible to derive possible locations of frost from results of the extended model. Refining the crude representation of winter services would lead to further improvements.
575 The extended model provides the opportunity to perform more realistic simulations of a winter event, where precipitation and obstacles are explicitly resolved. The effects of snow cover and precipitation especially on radiation are better represented. The extended model allows first estimates on influence of different city characteristics on snow heterogeneities. In the future, this information can be used for analyses on frost heterogeneities or human comfort. A sensitivity study extended for an urban neighbourhood is a next step to investigate, how obstacles influence the falling of snow and urban temperature development.

580   List of symbols

A_t	parameter for the rain droplet spectrum
a_mc	parameter for $a_\mathrm{m}(T)$ ($0.08\,\mathrm{kg\,m^{-2}}$)
a_mv	parameter for $a_\mathrm{m}(T)$ ($0.02\,\mathrm{kg\,m^{-2}}$)
$a_\mathrm{m}(T)$	mass-size relation of snow
$B_\mathrm{acc}^\mathrm{c}$	accretion rate (ice scheme)
$B_\mathrm{acc}^\mathrm{w}$	accretion rate (warm rain scheme)
B_au^c	autoconversion rate (ice scheme)
B_au^w	autoconversion rate (warm rain scheme)
B_cfrz	contact nucleation rate
B_cond	condensation rate
B_dep	deposition rate
B_evap	evaporation rate
bh	roof height
B_ifrz	immersion freezing rate
B_melt	melting rate
B_nuc	nucleation rate
B_rim	riming rate
B_she	shedding rate
B^*	heat conduction parameter
ν_ice	thermal conductivity of ice
c_p	specific heat of dry air at constant pressure
ν_snow	thermal conductivity of snow
ν_soil	thermal conductivity of soil
c_ice	specific heat capacity of ice
$c_\mathrm{v,snow}$	volumetric heat capacity of snow
D	threshold value for relative deviation
D_VDI	threshold value for relative deviation for wind speed following VDI (2017) (0.05)
E	rate of evaporation on ground
E_cf	collection efficiency ($5.0\cdot10^{-3}$)
F	correction factor
F_v	ventilation factor
$\overline{F}_{\overline{\phi}}$	diffusion term
$\overline{F}_{\overline{\phi},\dot{x}^1}$	diffusion term in x-direction

G_{soil}	heat flux to soil
h	orography height
H_{S}	sensible heat flux
h_{snow}	depth of daily temperature wave in snow
h_{soil}	depth of daily temperature wave in soil
i	location index
K_{hor}	horizontal exchange coefficient
K_{ver}	vertical exchange coefficient
$k_{\text{cold}}^{\text{s}}$	inverse autoconversion interval for snow ($10^{-3}\,\text{s}^{-1}$)
$k_{\text{cold}}^{\text{r}}$	inverse autoconversion interval for rain in ice scheme ($10^{-4}\,\text{s}^{-1}$)
k_{snow}	thermal diffusivity in snow
k_{soil}	thermal diffusivity in soil
$k_{\text{warm}}^{\text{r}}$	inverse autoconversion interval for rain in warm rain scheme ($10^{-3}\,\text{s}^{-1}$)
L_{21}	latent heat of vaporisation
L_{31}	latent heat of sublimation
L_{32}	latent heat of fusion
LW_{net}	net surface long wave radiation
L_{S}	latent heat flux
M_{snow}	melting rate of SWE on ground
N	total number of compared values
$N_{\text{cf},0} = 2.0 \cdot 10^5$	concentration of natural contact ice nuclei active at -4°C at sea level
n_i	hit/ fail
O	observation/ older model version
P	precipitation amount on ground
Pd	prediction/ newer model version
p_0	basic state atmospheric pressure
p_{ref}	reference pressure ($100000\,\text{Pa}$)
p_{S}	atmospheric pressure on ground surface
$p_{\text{snow}_{z_0}}$	snow cover fraction
Pr_{snow}	rate of snowfall
q	hit rate
q_1^1	specific humidity
$q_{1,\text{sat}}^1$	saturation specific humidity over water
$q_{1,\text{sat,ice}}^1$	saturation specific humidity over ice
q_1^{2c}	cloud water content

$q_{1,\text{cri}}^{2c}$	critical value for autoconversion ($10^{-3}\,\text{kg}\,\text{kg}^{-1}$)
q_1^{2r}	rain water content
q_1^{3s}	snow water content
R	gas constant for dry air
S	saturation
SWE	snow water equivalent
SWE_crit	critical SWE ($0.05\,\text{m}$)
SW_net	net surface short wave radiation
T	temperature
T_0	freezing point ($273.16\,\text{K}$)
T_1	minimum temperature for mass-size relation of snow ($253.16\,\text{K}$)
T_2	minimum temperature for temperature function ($235.16\,\text{K}$)
$T_\text{h,soil}$	deep soil temperature
T_S	temperature on ground surface
t	time
u	wind in west-east direction
U_ref	reference wind speed
v	wind in south-north direction
v_TR	terminal velocity of rain
v_TS	terminal velocity of snow
W	threshold value for absolute deviation
W_VDI	threshold value for absolute deviation for wind speed following VDI (2017) ($0.01\,\text{m}\,\text{s}^{-1}$)
w	wind in vertical direction
x	horizontal coordinate in west-east direction in Cartesian coordinate system
$\dot{x}^1$	coordinate in terrain-following coordinate system
$\dot{x}^2$	coordinate in terrain-following coordinate system
$\dot{x}^3$	coordinate in terrain-following coordinate system
y	horizontal coordinate in south-north direction in Cartesian coordinate system
z	vertical coordinate in Cartesian coordinate system
z_0	roughness length
z_{0_ini}	initial z_0 without snow cover
z_{0_snow}	snow roughness length ($10^{-3}\,\text{m}$)
z_snow	snow depth
α	albedo
α_cf	contact nucleation factor ($1.55 \cdot 10^{-3}$)

α_cond	condensation parameter
α_dep	deposition factor
α_if	immersion freezing factor ($9.95 \cdot 10^{-5}$)
α_ini	initial α without snow cover
α_max	maximum α_snow (0.85)
α_melt	melting factor ($7.2 \cdot 10^{-6}$)
α_min	minimum α_snow (0.18)
$\alpha_\text{min,J14}$	minimum α_snow following Järvi et al. (2014) (0.18)
$\alpha_\text{min,V91}$	minimum α_snow following Verseghy (1991)(0.5)
α^*	grid volume
β	empirical factor for roughness length (0.408)
β_dep	deposition factor (13.0)
β_melt	melting factor (13.0)
ΔSWE	difference of SWE
ΔSW_net	difference of SW_net
Δt	time step
Δv	difference of v wind component
ϵ	very small number (10^{-6})
$\epsilon(T)$	temperature function
θ	potential temperature
ρ_0	basic state atmospheric density
ρ_ice	density of ice ($918.9\,\text{kgm}^-3$)
ρ_max	maximum ρ_snow ($300\,\text{kgm}^-3$)
ρ_min	minimum ρ_snow ($100\,\text{kgm}^-3$)
ρ_ref	reference density ($1.29\,\text{kgm}^{-3}$)
ρ_snow	snow pack density
ρ_w	density of water
τ	period of temperature wave ($86400\,\text{s}$)
τ_1	time period parameter ($86400\,\text{s}$)
τ_f	empirical parameter for ρ_snow (0.24)
$\tau_{\text{f},\alpha}$	empirical parameter for albedo (0.11)
$\tau_{\text{f},\alpha,\text{J14}}$	empirical parameter for albedo following Järvi et al. (2014) (0.11)
$\tau_{\text{f},\alpha,\text{V91}}$	empirical parameter for albedo following Verseghy (1991) (0.24)
τ_α	empirical parameter for albedo (0.18)
$\tau_{\alpha,\text{J14}}$	empirical parameter for albedo following Järvi et al. (2014) (0.18)

$\tau_{\alpha,\text{V91}}$	empirical parameter for albedo following Verseghy (1991) (0.008)
ϕ	any scalar quantity
ϕ_0	basic state part of ϕ
$\tilde{\phi},$	deviation of ϕ

Code and data availability. Currently the MITRAS source code is distributed upon request under the terms of a user agreement with the Mesoscale and Microscale Modeling (MeMi) working group at the Meteorological Institute, University of Hamburg (https//www.mi.uni-hamburg.de/memi). A copy of the user agreement is available upon request. Due to current copyright restrictions, users are requested to contact the corresponding authors to obtain access to the code free of charge for research purposes under a collaboration agreement
585   (metras@uni-hamburg.de).

Documentation for the M-SYS model system (Schlünzen et al., 2018a, b), in which MITRAS is included, is available online at https://www.mi.uni-hamburg.de/memi under "Numerical Models". A detailed description of MITRAS version 2 can be found in Salim et al. (2018).

The initialisation profiles for the model runs can be found in the supplement of this article. The simulations are published at the World
590   Data Center for Climate (WDCC), (Samsel et al., 2025). The scripts used for the analyses and plotting are archived on Zenodo (https://doi.org/10.5281/zenodo.15194835, Samsel (2025)).

Author contributions. KSS organised the paper and collected the contributions. HS coordinated the model development since the beginning and is with DG overall responsible for the model and its documentation. MB developed the snow cover parameterisation in the mesoscale model METRAS and provided KSS with code and help. KS contributed to the introduction. All authors reviewed and edited the paper.

595   *Competing interests.* The authors declare that they have no conflict of interest.

Acknowledgements. This work was financed within the framework of the Helmholtz Institute for Climate Service Science (HICSS), a co-operation between Climate Service Center Germany (GERICS) and University Hamburg, Germany, and conducted as part of the WINTER project (Investigating climate change related impacts on the urban winter climate of Hamburg). This work was partly funded by the Deutsche Forschungsgemeinschaft (DFG, German Research Foundation) under Germany's Excellence Strategy – EXC 2037 'CLICCS – Climate, Cli-
600   matic Change, and Society' – Project Number: 390683824. The work contributes to the Center for Earth System Research and Sustainability (CEN) of University of Hamburg.

References

Arakawa, A. and Lamb, V. R.: Computational Design of the Basic Dynamical Processes of the UCLA General Circulation Model, Method. Comput. Phys., 17, 173–265, https://doi.org/10.1016/b978-0-12-460817-7.50009-4, 1977.

605 Asai, T.: A Numerical Study of the Air-Mass Transformation over the Japan Sea in Winter, Journal of the Meteorological Society of Japan. Ser. II, 43, 1–15, https://doi.org/10.2151/JMSJ1965.43.1_1, 1965.

Badeke, R., Matthias, V., and Grawe, D.: Parameterizing the vertical downward dispersion of ship exhaust gas in the near field, Atmospheric Chemistry and Physics, 21, 5935–5951, https://doi.org/10.5194/ACP-21-5935-2021, 2021.

Baker, D. G., Skaggs, R. H., and Ruschy, D. L.: Snow Depth Required to Mask the Underlying Surface, Journal of Applied Meteorology and
610 Climatology, 30, 387–392, https://doi.org/https://doi.org/10.1175/1520-0450(1991)030<0387:SDRTMT>2.0.CO;2, 1991.

Bergeron, O. and Strachan, I. B.: Wintertime radiation and energy budget along an urbanization gradient in Montreal, Canada, International Journal of Climatology, 32, 137–152, https://doi.org/10.1002/JOC.2246, 2012.

Bhumralkar, C. M.: Numerical Experiments on the Computation of Ground Surface Temperature in an Atmospheric General Circulation Model, Journal of Applied Meteorology and Climatology, 14, 1246–1258, https://doi.org/https://doi.org/10.1175/1520-
615 0450(1975)014<1246:NEOTCO>2.0.CO;2, 1975.

Boettcher, M.: Selected climate mitigation and adaptation measures and their impact on the climate of the region of Hamburg, PhD Thesis, University of Hamburg, Hamburg, Germany, 2017.

Bouteloup, Y., Seity, Y., and Bazile, E.: Description of the sedimentation scheme used operationally in all Météo-France NWP models, Tellus A, 63, 300–311, https://doi.org/10.1111/j.1600-0870.2010.00484.x, 2011.

620 Briscolini, M. and Santangelo, P.: Development of the mask method for incompressible unsteady flows, Journal of Computational Physics, 84, 57–75, https://doi.org/10.1016/0021-9991(89)90181-2, 1989.

Castelli, S. T. and Reisin, T. G.: Evaluation of the atmospheric RAMS model in an obstacle resolving configuration, Environmental Fluid Mechanics, 10, 555–576, https://doi.org/10.1007/s10652-010-9167-y, 2010.

Cox, R., Bauer, B. L., and Smith, T.: A Mesoscale Model Intercomparison, American Meteorological Society, 79, 265–284, 1998.

625 Deardorff, J. W.: Efficient prediction of ground surface temperature and moisture, with inclusion of a layer of vegetation, Journal of Geophysical Research: Oceans, 83, 1889–1903, https://doi.org/10.1029/JC083IC04P01889, 1978.

Doms, G.: Fluid- und Mikrodynamik in numerischen Modellen konvektiver Wolken, Inst. für Meteorologie und Geophysik der Univ. Frankfurt/Main, 1985.

Doms, G., Förstner, J., Heise, E., Herzog, H.-J., Mironov, D., Raschendorfer, M., Reinhardt, T., Ritter, B., Schrodin, R., Schulz, J.-P., and
630 Vogel, G.: A Description of the Nonhydrostatic Regional COSMO Model Part II : Physical Parameterizations, Deutscher Wetterdienst, Offenbach, Germany, www.cosmo-model.org, 2011.

Douville, H., Royer, J. F., and Mahfouf, J. F.: A new snow parameterization for the Météo-France climate model, Climate Dynamics, 12, 21–35, 1995.

Dutra, E., Balsamo, G., Viterbo, P., Miranda, P. M., Beljaars, A., Schar, C., and Elder, K.: An Improved Snow Scheme for the ECMWF Land
635 Surface Model: Description and Offline Validation, Journal of Hydrometeorology, 11, 899–916, https://doi.org/10.1175/2010JHM1249.1, 2010.

Eichhorn, J. and Kniffka, A.: The numerical flow model MISKAM: State of development and evaluation of the basic version, Meteorologische Zeitschrift, 19, 81–90, https://doi.org/10.1127/0941-2948/2010/0425, 2010.

Ferner, K. S., Boettcher, M., and Schlünzen, K. H.: Modelling the heterogeneity of rain in an urban neighbourhood with an obstacle-resolving model, Meteorologische Zeitschrift, https://doi.org/10.1127/metz/2022/1149, 2022.

Fischereit, J.: Influence of urban water surfaces on human thermal environments - an obstacle resolving modelling approach, PhD Thesis, University of Hamburg, Hamburg, Germany, 2018.

Franke, J., Sturm, M., and Kalmbach, C.: Validation of OpenFOAM 1.6.x with the German VDI guideline for obstacle resolving micro-scale models, Journal of Wind Engineering and Industrial Aerodynamics, 104-106, 350–359, https://doi.org/10.1016/J.JWEIA.2012.02.021, 2012.

Geletič, J., Lehnert, M., Resler, J., Krč, P., Middel, A., Krayenhoff, E. S., and Krüger, E.: High-fidelity simulation of the effects of street trees, green roofs and green walls on the distribution of thermal exposure in Prague-Dejvice, Building and Environment, 223, 109 484, https://doi.org/10.1016/J.BUILDENV.2022.109484, 2022.

Geleyn, J.-F., Catry, B., Bouteloup, Y., and Brožková, R.: A statistical approach for sedimentation inside a microphysical precipitation scheme, Tellus A: Dynamic Meteorology and Oceanography, 60, 649–662, https://doi.org/10.1111/j.1600-0870.2008.00323.x, 2008.

Grawe, D., Schlünzen, K. H., and Pascheke, F.: Comparison of results of an obstacle resolving microscale model with wind tunnel data, Atmospheric Environment, 79, 495–509, https://doi.org/10.1016/j.atmosenv.2013.06.039, 2013.

Grawe, D., Bächlin, W., Brünger, H., Eichhorn, J., Franke, J., Leitl, B., Müller, W., Öttl, D., Salim, M. H., Schlünzen, K. H., Winkler, C., and Zimmer, M.: An Updated Evaluation Guideline for Prognostic Microscale Wind Field Models, 9th International Conference on Urban Climate, Toulouse, France, 2015.

Gunn, K. L. S. and Marshall, J. S.: The Distribution with Size of Aggregate Snowflakes, Journal of Meteorology, 15, 452–461, https://doi.org/10.1175/1520-0469(1958)015<0452:tdwsoa>2.0.co;2, 1958.

Hirota, T., Pomeroy, J. W., Granger, R. J., and Maule, C. P.: An extension of the force-restore method to estimating soil temperature at depth and evaluation for frozen soils under snow, Journal of Geophysical Research Atmospheres, 107, ACL 11–1–ACL 11–10, https://doi.org/10.1029/2001JD001280, 2002.

Ho, C. L. and Valeo, C.: Observations of urban snow properties in Calgary, Canada, Hydrological Processes, 19, 459–473, https://doi.org/10.1002/HYP.5544, 2005.

Hu, C., Tam, C. Y., liang Yang, Z., and Wang, Z.: Analyzing urban influence on extreme winter precipitation through observations and numerical simulation of two South China case studies, Scientific Reports 2024 14:1, 14, 1–21, https://doi.org/10.1038/s41598-024-52193-2, 2024.

Järvi, L., Grimmond, C. S., Taka, M., Nordbo, A., Setälä, H., and Strachan, I. B.: Development of the Surface Urban Energy and Water Balance Scheme (SUEWS) for cold climate cities, Geoscientific Model Development, 7, 1691–1711, https://doi.org/10.5194/GMD-7-1691-2014, 2014.

Kessler, E.: On the Distribution and Continuity of Water Substance in Atmospheric Circulations, Meteorological Monographs, 10, https://doi.org/10.1007/978-1-935704-36-2, 1969.

Khain, A. P., Beheng, K. D., Heymsfield, A., Korolev, A., Krichak, S. O., Levin, Z., Pinsky, M., Phillips, V., Prabhakaran, T., Teller, A., Heever, S. C. V. D., and Yano, J. I.: Representation of microphysical processes in cloud-resolving models: Spectral (bin) microphysics versus bulk parameterization, Reviews of Geophysics, 53, 247–322, https://doi.org/10.1002/2014RG000468, 2015.

Köhler, A.: Parameterisierung der Wolkenmikrophysik und der Strahlung in einem mesoskaligen Transport- und Strömungsmodell, Diploma Thesis, University of Hamburg, Hamburg, Germany, 1990.

Lemonsu, A., Bélair, S., Mailhot, J., Benjamin, M., Chagnon, F., Morneau, G., Harvey, B., Voogt, J., and Jean, M.: Overview and First Results of the Montreal Urban Snow Experiment 2005, Journal of Applied Meteorology and Climatology, 47, 59–75, https://doi.org/10.1175/2007JAMC1639.1, 2008.

Lemonsu, A., Bélair, S., Mailhot, J., and Leroyer, S.: Evaluation of the Town Energy Balance Model in Cold and Snowy Conditions during the Montreal Urban Snow Experiment 2005, Journal of Applied Meteorology and Climatology, 49, 346–362, https://doi.org/10.1175/2009JAMC2131.1, 2010.

Liu, J. and Niyogi, D.: Meta-analysis of urbanization impact on rainfall modification, Scientific Reports, 9, https://doi.org/https://doi.org/10.1038/s41598-019-42494-2, 2019.

Lu, Y., Yu, Z., Albertson, J. D., Chen, H., Hu, L., Pendergrass, A., Chen, X., and Li, Q.: Understanding the Influence of Urban Form on the Spatial Pattern of Precipitation, Earth's Future, 12, e2023EF003 846, https://doi.org/10.1029/2023EF003846, 2024.

Malevich, S. B. and Klink, K.: Relationships between Snow and the Wintertime Minneapolis Urban Heat Island, Journal of Applied Meteorology and Climatology, 50, 1884–1894, https://doi.org/10.1175/JAMC-D-11-05.1, 2011.

Maronga, B., Gross, G., Raasch, S., Banzhaf, S., Forkel, R., Heldens, W., Kanani-Sühring, F., Matzarakis, A., Mauder, M., Pavlik, D., Pfafferott, J., Schubert, S., Seckmeyer, G., Sieker, H., and Winderlich, K.: Development of a new urban climate model based on the model PALM - Project overview, planned work, and first achievements, Meteorologische Zeitschrift, 28, 105–119, https://doi.org/10.1127/metz/2019/0909, 2019.

Maronga, B., Banzhaf, S., Burmeister, C., Esch, T., Forkel, R., Fröhlich, D., Fuka, V., Gehrke, K. F., Geletič, J., Giersch, S., Gronemeier, T., Groß, G., Heldens, W., Hellsten, A., Hoffmann, F., Inagaki, A., Kadasch, E., Kanani-Sühring, F., Ketelsen, K., Khan, B. A., Knigge, C., Knoop, H., Krč, P., Kurppa, M., Maamari, H., Matzarakis, A., Mauder, M., Pallasch, M., Pavlik, D., Pfafferott, J., Resler, J., Rissmann, S., Russo, E., Salim, M., Schrempf, M., Schwenkel, J., Seckmeyer, G., Schubert, S., Sühring, M., Tils, R. V., Vollmer, L., Ward, S., Witha, B., Wurps, H., Zeidler, J., and Raasch, S.: Overview of the PALM model system 6.0, Geoscientific Model Development, 13, 1335–1372, https://doi.org/10.5194/GMD-13-1335-2020, 2020.

Marshall, J. S. and Palmer, W. M.: The Distribution of Raindrops with Size, Journal of Meteorology, 5, 165–166, https://doi.org/https://doi.org/10.1175/1520-0469(1948)005<0165:TDORWS>2.0.CO;2, 1948.

Meinke, I., Rechid, D., Tinz, B., Maneke, M., Lefebvre, C., and Isokeit, E.: Klima der Region – Zustand, bisherige Entwicklung und mögliche Änderungen bis 2100, Hamburger Klimabericht – Wissen über Klima, Klimawandel und Auswirkungen in Hamburg und Norddeutschland, pp. 15–36, https://doi.org/10.1007/978-3-662-55379-4_2, 2018.

Mittal, R. and Iaccarino, G.: Immersed Boundary Methods, Annual Review of Fluid Mechanics, 37, 239–261, https://doi.org/10.1146/annurev.fluid.37.061903.175743, 2005.

Mori, K. and Sato, T.: Evaluating the Role of Snow Cover in Urban Canopy Layer on the Urban Heat Island in Sapporo, Japan with a Regional Climate Model, Journal of the Meteorological Society of Japan. Ser. II, 93, 581–592, https://doi.org/10.2151/JMSJ.2015-039, 2015.

Pielke, R. A.: Mesoscale Meteorological Modeling, Academic Press, 3rd edn., 2013.

Pielke, R. A., Cotton, W. R., Walko, R. L., Tremback, C. J., Lyons, W. A., Grasso, L. D., Nicholls, M. E., Moran, M. D., Wesley, D. A., Lee, T. J., and Copeland, J. H.: A comprehensive meteorological modeling system - RAMS, Meteorology and Atmospheric Physics, 49, 69–91, https://doi.org/10.1007/BF01025401, 1992.

Purr, C., Brisson, E., and Ahrens, B.: Convective rain cell characteristics and scaling in climate projections for Germany, International Journal of Climatology, 41, 3174–3185, https://doi.org/10.1002/JOC.7012, 2021.

Roeckner, E., Baeuml, G., Bonventura, L., Brokopf, R., Esch, M., Giorgetta, M., Hagemann, S., Kirchner, I., Kornblueh, L., Manzini, E.,
715   Rhodin, A., Schlese, U., Schulzweida, U., and Tompkins, A. K.: The atmospheric general circulation model ECHAM5. PART I: Model
       description, Max Planck Institute for Meteorology, Hamburg, Germany, 2003.

Salim, M. H., Schlünzen, K. H., Grawe, D., Boettcher, M., Gierisch, A. M., and Fock, B. H.: The microscale obstacle-resolving meteorolog-
       ical model MITRAS v2.0: Model theory, Geoscientific Model Development, 11, 3427–3445, https://doi.org/10.5194/gmd-11-3427-2018,
       2018.

720   Salvi, K. A. and Kumar, M.: Imprint of urbanization on snow precipitation over the continental USA, Nature Communications 2024 15:1,
       15, 1–11, https://doi.org/10.1038/s41467-024-46699-6, 2024.

Samsel, K. S.: Analysis and plotting scripts supporting: "A method for assessing model extensions: Application to modelling winter pre-
       cipitation with a microscale obstacle-resolving meteorological model (MITRAS v4.0)", Zenodo [Code], https://doi.org/10.5281/zenodo.
       15194835, 2025.

725   Samsel, K. S., Boettcher, M., Grawe, D., Schlünzen, K. H., and Sieck, K.: Simulations for assessing model extensions using an obstacle-
       resolving model, https://www.wdc-climate.de/ui/entry?acronym=WINTER_HAM_MitrasModEx, 2025.

Schatz, J. and Kucharik, C. J.: Seasonality of the Urban Heat Island Effect in Madison, Wisconsin, Journal of Applied Meteorology and
       Climatology, 53, 2371–2386, https://doi.org/10.1175/JAMC-D-14-0107.1, 2014.

Schatzmann, M., Bächlin, W., Emeis, S., Kühlwein, J., Leitl, B., Müller, W. J., Schäfer, K., and Schlünzen, H.: Development and validation
730   of tools for the implementation of European air quality policy in Germany (Project VALIUM), Atmospheric Chemistry and Physics, 6,
       3077–3083, https://doi.org/10.5194/acp-6-3077-2006, 2006.

Schlünzen, K. and Sokhi, R., eds.: Overview of Tools and Methods for Meteorological and Air Pollution Mesoscale Model Evaluation and
       User Training. Joint Report of COST Action 728 and GURME, GAW Report 181, World Meteorological Organization (WMO), Geneva,
       Switzerland, https://library.wmo.int/idurl/4/47523, 2008.

735   Schlünzen, K. H., Hinneburg, D., Knoth, O., Lambrecht, M., Leitl, B., López, S., Lüpkes, C., Panskus, H., Renner, E., Schatzmann, M.,
       Schoenemeyer, T., Trepte, S., and Wolke, R.: Flow and transport in the obstacle layer: First results of the micro-scale model MITRAS,
       Journal of Atmospheric Chemistry, 44, 113–130, https://doi.org/10.1023/A:1022420130032, 2003.

Schlünzen, K. H., Boettcher, M., Fock, B. H., Gierisch, A., Grawe, D., and Salim, M.: Scientific Documentation of the Multiscale Model
       System M-SYS, Meteorologisches Institut, University of Hamburg, MeMi Technical Report 4, p. 153 pp., 2018a.

740   Schlünzen, K. H., Boettcher, M., Fock, B. H., Gierisch, A., Grawe, D., and Salim, M.: Technical Documentation of the Multiscale Model
       System M-SYS, Meteorologisches Institut, University of Hamburg, MeMi Technical Report 3, p. 136 pp., 2018b.

Shui, T., Liu, J., Zhang, P., Liu, S., and Zhao, Z.: Development of an urban canopy model for the evaluation of urban thermal climate with
       snow cover in severe cold regions, Building and Environment, 95, 160–170, https://doi.org/10.1016/J.BUILDENV.2015.09.016, 2016.

Shui, T., Liu, J., Xiao, Y., and Shi, L.: Effects of snow cover on urban surface energy exchange: Observations in Harbin, China during the
745   winter season, International Journal of Climatology, 39, 1230–1242, https://doi.org/10.1002/JOC.5873, 2019.

Smoliak, B. V., Snyder, P. K., Twine, T. E., Mykleby, P. M., and Hertel, W. F.: Dense Network Observations of the Twin Cities Canopy-Layer
       Urban Heat Island, Journal of Applied Meteorology and Climatology, 54, 1899–1917, https://doi.org/10.1175/JAMC-D-14-0239.1, 2015.

Trukenmüller, A., Grawe, D., and Schlünzen, K. H.: A model system for the assessment of ambient air quality conforming to EC directives,
       Meteorologische Zeitschrift, 13, 387–394, https://doi.org/10.1127/0941-2948/2004/0013-0387, 2004.

750   Uphoff, M.: Einflüsse von Wolkeneffektparametrisierung und Modellauflösung auf simuliertes bodennahes Ozon, PhD Thesis, University of
       Hamburg, Hamburg, Germany, https://ediss.sub.uni-hamburg.de/handle/ediss/6167, 2019.

VDI: Environmental meteorology - Prognostic microscale wind field models - Evaluation for flow around buildings and obstacles, Technical Report, VDI Guideline 3783, Blatt 9, 2017.

Verseghy, D. L.: Class—A Canadian land surface scheme for GCMS. I. Soil model, International Journal of Climatology, 11, 111–133, https://doi.org/10.1002/JOC.3370110202, 1991.

von Salzen, K., Claussen, M., and Schlünzen, K. H.: Application of the concept of blending height to the calculation of surface fluxes in a mesoscale model, Meteorologische Zeitschrift, 5, 60–66, https://doi.org/10.1127/METZ/5/1996/60, 1996.

Watanabe, N., Setoguchi, T., Maeda, K., Iwakuni, D., Guo, Z., and Tsutsumi, T.: Sustainable Block Design Process for High-Rise and High-Density Districts with Snow and Wind Simulations for Winter Cities, Sustainability, 9, 2132, https://doi.org/10.3390/SU9112132, 2017.

WMO: Guide to Instruments and Methods of Observation Volume I - Measurement of Meteorological Variables, 2023 edition, WMO-No. 8, World Meteorological Organization (WMO), Geneva, Switzerland, https://library.wmo.int/idurl/4/68695, 2023.

Zhang, Q., Zhang, Y., Yin, Z., Zhang, G., Mo, H., and Fan, F.: Experimental Study of Interference Effects of a High-Rise Building on the Snow Load on a Low-Rise Building with a Flat Roof, Applied Sciences 2021, 11, 11 163, https://doi.org/10.3390/APP112311163, 2021.

Zhang, W., Yang, J., Yang, L., and Niyogi, D.: Impacts of City Shape on Rainfall in Inland and Coastal Environments, Earth's Future, 10, e2022EF002 654, https://doi.org/10.1029/2022EF002654, 2022.

Zhou, X., Liu, Z., Ma, W., Kosugi, K., and Gu, M.: Experimental investigation of snow drifting on flat roofs during snowfall: Impact of roof span and snowfall intensity, Cold Regions Science and Technology, 190, 103 356, https://doi.org/10.1016/J.COLDREGIONS.2021.103356, 2021.